

Modular Jump Gaussian Processes

Anna R. Flowers* Christopher T. Franck† Mickaël Binois‡ Chiwoo Park§
Robert B. Gramacy†

November 21, 2025

Abstract

Gaussian processes (GPs) furnish accurate nonlinear predictions with well-calibrated uncertainty. However, the typical GP setup has a built-in stationarity assumption, making it ill-suited for modeling data from processes with sudden changes, or “jumps” in the output variable. The “jump GP” (JGP) was developed for modeling data from such processes, combining local GPs and latent “level” variables under a joint inferential framework. But joint modeling can be fraught with difficulty. We aim to simplify by suggesting a more modular setup, eschewing joint inference but retaining the main JGP themes: (a) learning optimal neighborhood sizes that locally respect manifolds of discontinuity; and (b) a new cluster-based (latent) feature to capture regions of distinct output levels on both sides of the manifold. We show that each of (a) and (b) separately leads to dramatic improvements when modeling processes with jumps. In tandem (but without requiring joint inference) that benefit is compounded, as illustrated on real and synthetic benchmark examples from the recent literature.

Keywords: computer experiment, nonstationarity, latent variable, local neighborhoods, mixture model

1 Introduction

We consider processes $Y(x) : \mathbb{R}^d \rightarrow \mathbb{R}$ that are smooth for most of the surface except along a manifold of discontinuity which spatially¹ partitions the response $Y(x)$ into two levels depending on x . One example of such a process is a computer simulation of an automated material handling vehicle (AMHV) transport system measuring the average transport time $Y(x)$ of material transport devices given their characteristics x (Park et al., 2023). Usually, transport time is low, but when the devices are working at or near capacity transport time suddenly increases – it “jumps”. Other examples of jump dynamics exist in geostatistics (Kim et al., 2005), physiology (Vieth, 1989), ecology (Toms and Lesperance, 2003), and materials science (Park et al., 2022). We narrow our focus to jumps exhibited by computer simulation experiments, where $Y(x)$ models complex phenomena as a deterministic function of inputs x at potentially great computational expense, although we expect our idea to be applicable to any data with jumps in the response. In this paper we consider jump processes with only two levels.

When designing computer simulation experiments, one often meta-models a planned experiment of runs of the computer model. That is, gather a collection of N data pairs $(x_1, y_1), \dots, (x_N, y_N)$, where $y_i = Y(x_i)$, and obtain a fit that can predict $Y(x)$ at new inputs. Such *surrogate models* (Santner et al., 2003; Gramacy, 2020) are instrumental to many applications where ready access to runs of the computer model are unavailable or expensive. The canonical surrogate is a Gaussian process (GP; e.g., Sacks et al.,

*Corresponding author: Department of Statistics, Virginia Tech, arflowers@vt.edu

†Department of Statistics, Virginia Tech

‡Université Côte d’Azur, Inria, CNRS, LJAD, France

§Department of Industrial and Systems Engineering, University of Washington

¹Throughout the paper, we use “spatial” with reference to the input space, not “geospatial” locations on Earth.

1989) because GPs furnish accurate nonlinear predictions with good uncertainty quantification. For this reason they are also popular for many regression applications in machine learning (e.g., Rasmussen and Williams, 2006) and geospatial settings (e.g., Banerjee et al., 2004), where GPs are known as “kriging” (Schabenberger and Gotway, 2017; Zimmerman and Ver Hoef, 2024). There are two downsides to GP modeling in many contexts. One is that computational demands for inference scale poorly as N gets large; another is that the typical GP formulation assumes stationarity, in that only relative distances between input locations matter. This means GPs struggle to capture dynamics where modeling fidelity varies in the input space, e.g., where one part is flat and another is wiggly. GPs also struggle if there are jumps of discontinuity in which the level of the response drastically changes.

There is a sizable literature on nonstationary GP modeling. Sauer et al. (2023a) provide a recent review. Many such approaches involve imposing hard partitions in the input space (e.g., Kim et al., 2005; Pope et al., 2021; Payne et al., 2020; Gramacy and Lee, 2008; Luo et al., 2023), which could potentially cope with jumps that are axis aligned (like with trees) or are polygonal (Voronoi tessellations). Other approaches involve smoothly warping the inputs into a stationary regime (e.g., Sampson and Guttorp, 1992; Schmidt and O’Hagan, 2003; Damianou and Lawrence, 2013; Sauer et al., 2023b), which is often better but would struggle with discontinuity. GPs exist which can handle discontinuities (e.g., Garnett et al., 2010; Picheny et al., 2019), but they do not assume the response contains distinct levels. Park (2022) created the “jump GP” (JGP) specifically for data from processes that are piecewise continuous in order to address this gap. JGPs have three main modeling ingredients that are tightly coupled together. The first two are local (GP) modeling (e.g., Gramacy and Apley, 2015), and latent component (i.e., output level) membership variables. Inference is joint over all unknowns – in particular for the high dimensional latent variable – via modern variants of expectation maximization (EM; Dempster et al., 1977), comprising the third ingredient. JGP is a clever, but complex, modeling apparatus that works well out-of-sample when trained on data from response surfaces exhibiting jumps.

Here we suggest that the essence of a JGP can be extracted by appropriating its main ingredients in a more modular setup. We still use local modeling, latent variables, and clustering via EM, but we avoid joint inference and instead do things one step at a time by daisy-chaining off-the-shelf subroutines. To explain, consider a simple illustrative example of a process with jumps in 1d.

$$Y(x) = \begin{cases} \sin(x) & x < 50 \\ \sin(x) + 10 & 50 \leq x < 70 \\ \sin(x) & x \geq 70 \end{cases} \quad (1)$$

So $Y(x)$ follows a simple sinusoid but jumps up by 10 between $x = 50$ and $x = 70$. Each panel of Figure 1 shows $Y(x)$ as a solid black line with a different “fit” from data $(x_1, y_1), \dots, (x_N, y_N)$. We use $N = 100$ inputs x_i chosen via Latin hypercube sample (LHS; McKay et al., 1979). These are not shown to reduce clutter. Figure 1 was produced with standard libraries and default settings, detailed in Section 5.

The top left panel of Figure 1 shows an ordinary/stationary GP fit, as reviewed in Section 2.1. Three issues are of note here: the GP is mistaking signal for noise, overestimating variance, and smoothing over the jumps. It seems to only have detected signal from the jumps, not from the sinusoid. Uncertainty is uniform because inputs are uniform and the GP assumes stationarity. Now turn to the top right panel, showing a local (approximate) GP (LAGP), reviewed in Section 2.2. For now we remark that a LAGP is basically an ordinary GP where training data far from the testing location(s) is not used. Less data means faster calculations and increased “reactivity” if dynamics change in the input space. Notice how LAGP shows an improvement over the ordinary GP (top left) for $x < 40$ and $x > 80$. Signal is detected there, and variance is much reduced. But this comes at the expense of accuracy in the middle region, and near

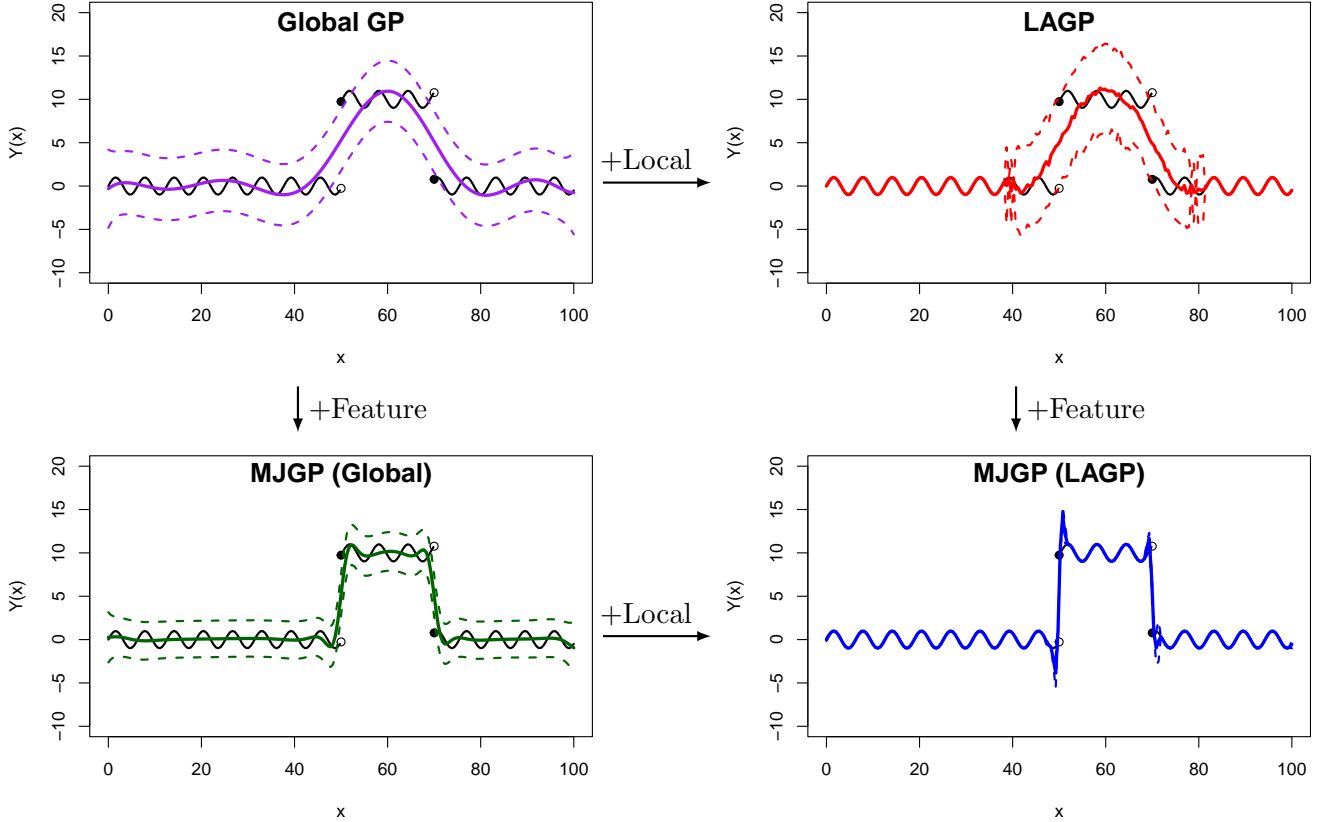


Figure 1: All panels show true function $Y(x)$ from Eq. (1) in black. Colored lines represent the mean (solid) and 95% PI (dashed) via (top left) a global GP, (top right) LAGP, (bottom left) MJGP with global GP, and (bottom right) MJGP with LAGP. Training data not shown.

the “jumps” on either side. Uncertainty here is inflated relative to the stationary GP fit. Importantly, LAGP uses a fixed-sized neighborhood of locality ($n = 25$) everywhere in the input space which we shall explain in more detail in Section 2.2. Our proposed approach improves upon this by dynamically selecting the optimal neighborhood size throughout the input space as described in Section 3.

The lower panels of Figure 1 highlight our main contribution. Focus first on the lower-left. Suppose we were to cluster the observations marginally. We ignore (x_1, \dots, x_N) and use an unsupervised learning scheme to assign (one of two) labels to each of (y_1, \dots, y_N) . In this 1d example, most clustering methods will easily partition these y -values into components around 0 and 10. We use model-based clustering via EM for this, as described in Section 4.2, but suggest several variations and other approaches that often work just as well. Using cluster memberships, e.g., $c_i = 1$ for y_i around 0 and $c_j = 2$ for y_j around 10, suppose we were to learn a classification rule spatially for pairs $(x_1, c_1), \dots, (x_N, c_N)$, i.e., reincorporating the inputs (x_1, \dots, x_N) with supervised learning. There are again many choices for this; we prefer a classification GP (CGP). This allows us to predict a probability of class 2 at x , in-sample at (x_1, \dots, x_N) yielding (p_1, \dots, p_N) , or out-of sample for testing as $p(x)$. We then treat the class predictions $(p_1 \dots p_N)$, derived from the training data, as an input feature in our GP fit. That is, take the same GP from the top-left panel, but train it on input tuple (x_i, p_i) and output y_i , for $i = 1, \dots, N$. When predicting, augment any testing x with $p(x)$ for tuple $(x, p(x))$. This global GP with the new feature is visualized in the lower

left panel of Figure 1. Notice how the fit tracks the jumps better (compared to the top left), and it is more confident everywhere, but it still struggles to pick up on the sinusoid. The idea of learning an auxiliary input feature to accommodate nonstationarity is not new (Bornn et al., 2012) but, like Park et al. (2022) for JGP, Bornn et al. perform joint inference for the GP and the latent quantity, which can be cumbersome. A key feature of our approach is that we do everything in a pre-processing step with off-the-shelf libraries. This both increases the flexibility of our approach and makes it more widely accessible.

Finally, the bottom right panel of Figure 1 combines the feature with local modeling: LAGP applied on (x_i, p_i) and output y_i , but otherwise the same as the feature-expanded GP on the left. We call this the Modular JGP (MJGP). Except for some elevated uncertainty near the jump points, which is sensible, the fit is nearly perfect: high accuracy, low variance. In the remainder of the paper our goal is to flesh out these ideas, making them more concrete, especially as regards implementation. We begin with review in Section 2. We then describe our main methodological contributions in Sections 3 and 4: optimizing local neighborhoods and cluster-based features. Throughout, we provide illustrations on examples that have the same spirit as Figure 1, but are more realistic. Section 5 provides empirical benchmarking exercises in several variations including on a real simulation from manufacturing. Finally, Section 6 concludes with a brief discussion of limitations and possible future work. All code is provided via Git: <https://bitbucket.org/gramacylab/jumpgp>.

2 Review

Here we provide a brief review of GPs and a popular variant, LAGP.

2.1 Gaussian Processes

Let X_N be an $N \times d$ matrix of input features and Y_N be a corresponding $N \times 1$ vector of outputs. We assume X_N has been pre-scaled to the unit d -cube. Additionally, let x_i^\top denote the i^{th} row of X_N . We consider estimating an unknown function via training data X_N and Y_N using a GP (Rasmussen and Williams, 2006; Gramacy, 2020). A typical GP prior implies that $Y_N \sim \mathcal{N}(\mu, \Sigma(X_N))$, where μ is often assumed to be 0 so that all of the modeling “action” is in $\Sigma(X_N)$. This setup induces a likelihood function:

$$L(Y_N | X_N) \propto |\Sigma(X_N)|^{-\frac{1}{2}} \exp \left\{ -\frac{1}{2} Y_N^\top \Sigma(X_N)^{-1} Y_N \right\}. \quad (2)$$

The likelihood (2) can be used to learn $\Sigma(X_N)$ under some restrictions, such as positive definiteness. Often, covariance is built from a kernel specifying $\Sigma(X_N)_{ij} = \Sigma(x_i, x_j)$. Kernels that depend only on the distance between inputs yield stationary processes, eliminating all input position information from the model. One example is squared exponential kernel

$$\Sigma(X_N)_{ij} = \Sigma(x_i, x_j) = \tau^2 \exp \left\{ -\sum_{k=1}^d \frac{\|x_{ik} - x_{jk}\|^2}{\theta_k} \right\}, \quad (3)$$

which we use throughout, although none of our contribution is explicitly tied to this choice. Other stationary kernels, such as Matérn (Stein, 2012), are similarly appropriate. Above, τ^2 and $\theta = [\theta_1, \dots, \theta_d]$ are hyperparameters representing the scale and lengthscale, respectively. These quantities may be inferred via maximum likelihood estimation (MLE) with Eq. (2).

The same structure may be extended from training to testing for prediction. Let \mathcal{X} denote an $m \times d$ matrix of new/testing locations, and \tilde{x}_i^\top be the i^{th} row of \mathcal{X} . Then, using any hyperparameters learned

from training data, $Y(\mathcal{X}) | X_N, Y_N \sim \mathcal{N}_m(\mu_N(\mathcal{X}), \Sigma_N(\mathcal{X}))$ where

$$\begin{aligned} \mu_N(\mathcal{X}) &= \Sigma(\mathcal{X}, X_N)\Sigma(X_N)^{-1}Y_N, & \text{using } \Sigma(\mathcal{X}, X_N)_{ij} &= \Sigma(\tilde{x}_i, x_j), \\ \text{and } \Sigma_N(\mathcal{X}) &= \Sigma(\mathcal{X}) - \Sigma(\mathcal{X}, X_N)\Sigma(X_N)^{-1}\Sigma(\mathcal{X}, X_N)^\top. \end{aligned} \quad (4)$$

As a shorthand for later, let $\text{GP}(\mathcal{X}; X_N, Y_N)$ indicate the use of Eqs. (2–4) to represent predictions at \mathcal{X} via MLE hyperparameters using training data X_N and Y_N . We refer to this as a “global GP” since all training data are used. Such a fit is valid for prediction at any \mathcal{X} in the input space. This is in contrast to a GP fit using a subset of the training data, which we shall review next. The GP shown in the top left panel of Figure 1 is a global GP, where the solid purple line is $\mu_N(\mathcal{X})$ and the dashed purple line is a 95% prediction interval (PI) calculated using the diagonal entries of $\Sigma_N(\mathcal{X})$.

A global GP has two drawbacks: computation becomes prohibitive as N increases, and it does not perform well when training data come from nonstationary processes. The first can be seen by noting $\Sigma(X_N)^{-1}$ and $|\Sigma(X_N)|$ in Eqs. (2) and (4), both $\mathcal{O}(N^3)$ operations. To see the second, refer back to the discussion of Figure 1 (top-left), illustrating fits on a process with jumps. Consider a single data point at $x = 45$, which is part of the level-0 region. The issue with the global GP setup is that two equidistant points, say $x = 35$ and 55 , generate the same covariance, even though one point is in the level-0 region and the other is in the level-10 region. However notice that the data is locally stationary, in three spatial regimes, which suggests a divide-and-conquer approach may work well.

2.2 Local Approximate Gaussian Processes

LAGP (Gramacy and Apley, 2015) tackles both drawbacks at once: computational expense and stationarity. Observe from Eq. (3) that for two locations x_i and x_j , $\Sigma(x_i, x_j) \rightarrow 0$ as $\|x_i - x_j\| \rightarrow \infty$. Consider a single new location x where we wish to make a prediction, e.g., a single row of \mathcal{X} in Section 2.1. Note in Eq. (4) that $\Sigma(x, X_N)$ serves as a weight for $\mu_N(\mathcal{X})$; thus, any training y_i whose x_i is far from x has little influence on $\mu_N(\mathcal{X})$. Recognizing this, LAGP chooses a subset of $n \ll N$ “useful” data points $X_n(x) \subset X_N$ to predict x . There are many ways to define “useful”, such as nearest neighbors (NN), mean-squared predictive error, and Fisher information. Throughout we consider LAGP via NN, although it could be worth entertaining other criteria as we discuss briefly in Section 6. LAGP is not unique in its use of a small selection nearby points. Other, similar methods include nearest neighbor GPs (Datta et al., 2016a,b), inducing points (Snelson and Ghahramani, 2005; Banerjee et al., 2008), or kernels and basis functions with compact support (Nychka et al., 2015; Kaufman et al., 2011). However, LAGP is unique in its focus on points nearby to the predictive location x , as opposed to globally or for all X_N .

The core idea behind LAGP is that fitting a GP to $X_n(x) \subset X_N$ with $n \ll N$, along with corresponding Y_n , is both faster, and more reactive to local dynamics around x . We encapsulate that in shorthand as $\text{LAGP}_n(x) = \text{GP}(x; X_n(x), Y_n)$ after optimizing any hyperparameters in $\Sigma(X_n(x))$, and $\text{LAGP}_n(\mathcal{X})$ for m separate applications covering all of \mathcal{X} . The top right panel of Figure 1 shows $\text{LAGP}_{25}(\mathcal{X})$, where the red solid line denotes $\mu_N(\mathcal{X})$ and the red dashed line denotes a 95% PI. Since calculations are computationally exclusive for each $x \in \mathcal{X}$, we do not get a full covariance structure $\Sigma_N(\mathcal{X})$, only a diagonal one with entries σ_x^2 . The upside, though, is that the calculations are massively parallelizable (Gramacy et al., 2014).

LAGP reduces computational costs from $\mathcal{O}(N^3)$ to $\mathcal{O}(n^3)$, offering substantial speedups if $n \ll N$. Much work has been done to further decrease the computation time for fixed neighborhood size n (Gramacy and Haaland, 2016; Sung et al., 2018; Cole et al., 2021). Besides being faster, LAGP may also be more accurate for data from a nonstationary process. To see this, refer again to Figure 1 (top-right). By excluding points that are far from each x , LAGP has captured local trends (at least for the $x < 40$ or $x > 80$ regions) better than the global GP (top-left). However, LAGP does not perform well in the $40 < x < 80$ region. This is

because these predictive locations have neighbors from across the jumps.

To explore a potential remedy, consider a higher-dimensional illustration. Figure 2 depicts a simple

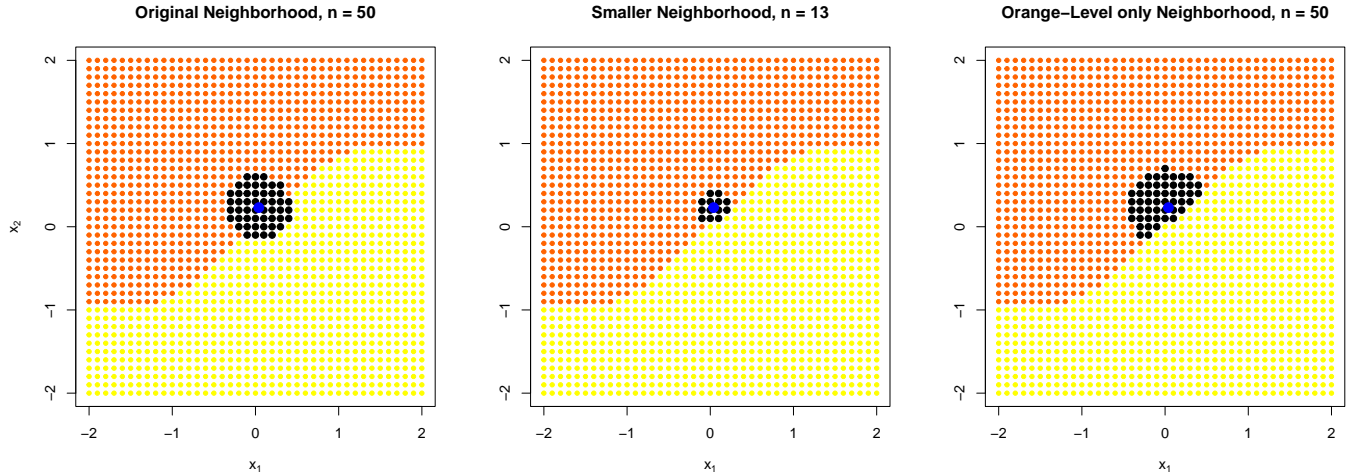


Figure 2: Three possible neighborhood choices for $x = (0.04, 0.023)$ (the blue dot). The two colors (orange and yellow) are two levels of the response, with a manifold of discontinuity at $\sin(x_1) = x_2$. The orange and yellow dots are X_N and the black dots are three different choices for $X_n(x)$.

manifold of discontinuity with two output values, orange and yellow, observed on an X_N grid. Now consider predicting at $x = (0.04, 0.23)$, in blue, using LAGP. Some potential neighborhoods $X_n(x)$ are depicted in black, one in each panel. The left panel uses Euclidean NNs with $n = 50$, but many such neighbors come from the opposite side of the manifold. One workaround is to shrink the neighborhood size, e.g., $n = 13$ in the center panel, which is the largest n that only contains neighbors from the orange region. So the choice of n implies a tradeoff between accuracy and reactivity. It could be advantageous to have a larger neighborhood (e.g., $n = 50$), but comprised of only orange points, as shown in the right panel.

3 Optimal Neighborhood-size LAGP

We turn now to the neighborhoods depicted in the center [this section] and right [Section 4] panels of Figure 2, respectively. The idea is to make adjustments near a manifold of discontinuity without affecting modeling dynamics elsewhere. To aid illustrations, Figure 3 borrows an example from Park (2022), known as “Phantom” data, with details in Appendix A.1. The image on the left is formed by evaluating the test function on a dense 101×101 grid in $[-0.5, 0.5]^2$. All responses (y -values) are deterministic. Observe that there is smooth color variation within the (mostly) red and yellow regions, revealing a strong signal locally (light reds and dark yellows, respectively), even away from the “jumps”. The histogram on the right helps understand the magnitudes of these signals. Notice that red and yellow regimes have comparable within-color variability and they are well-separated, with no values between 0.4 and 0.6.

The visuals in the panels of Figure 2 could represent zoomed-in versions of any of the jumps separating red from yellow in the left panel of Figure 3. Here, in Section 3, we present the first prong, which targets finding the optimal $n(x)$ for LAGP [Figure 2, middle] using its default, radial topography. The right panel of Figure 2, morphing that topography, represents the second prong and is the subject of Section 4. While jumps naturally focus interest on inputs near the manifold, the value of dynamically determining $n(x)$ for LAGP (other than the software default of $n = 50$) is not limited to those areas only. Intuitively, regions of

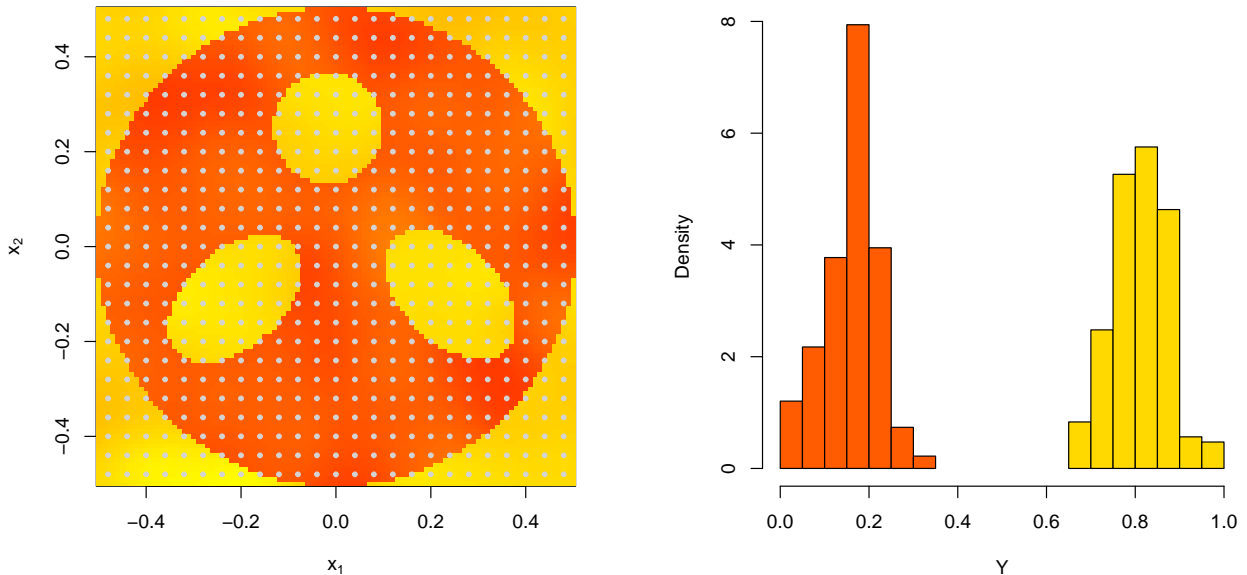


Figure 3: *Left*: True “Phantom” with training grid in gray; *Right*: Histogram of the marginal response.

slowly varying response should benefit from larger neighborhoods, whereas ones where it is changing more rapidly (via jump or not) should benefit from the greater reactivity provided by a smaller one.

3.1 Searching via validation

Consider a single predictive location x and a set of possible neighborhood sizes $n \equiv n(x) \in \{n_{\min}, \dots, n_{\max}\}$. We wish to estimate an optimal $\hat{n}(x)$ by some criterion, where $X_{n_{\min}}(x) \subseteq X_{\hat{n}}(x) \subseteq X_{n_{\max}}(x) \subseteq X_N$, as solved by LAGP [Section 2.2]. Let $\mu_n(x)$ denote the predictive mean under some $X_n(x)$, i.e., following Eq. (4), but conditional on $(X_n(x), Y_n)$. This prediction has some accuracy, say measured by squared error $\text{SE}(y, \mu_n(x))$, where y is the true but unknown value of the response at x . Generically, $\text{SE}(y, \hat{y}) = (y - \hat{y})^2$. One of the main contributions of Gramacy and Apley (2015) involves arguing that NN-constructed $X_n(x)$, conditional on a neighborhood size n , approximately minimizes the expectation of this quantity (i.e., the mean-squared error) for y following a stationary GP.

Here, we wish to extend that to choosing the best \hat{n} . However, we cannot use MSE under a stationary GP for y . There are two reasons for this. One is practical: this is not the case we are interested in – our jump processes are nonstationary. The other is more fundamental. If the process is stationary, then MSE is a decreasing function of the subset size n . In other words, you want to condition on as much data as possible. Since large n is generally intractable, Gramacy and Apley recommended choosing n as large as computational constraints allow. However, they observed that performance varied with n when the data exhibited telltale signs of nonstationarity, leaving an open question about what to do in practice. So instead of averaging SE, we create a validation exercise which allows us to plug-in an actual y_i value from the training data as a proxy.

Let x_* be the input in X_N that is closest (in terms of Euclidean distance) to x . Note that this is also the closest point to x in any $X_n(x)$ for $n \geq 1$ and that $x_* \equiv X_1(x)$. For ease of notation, we shall henceforth refer to $X_1(x)$ as x_* . Analogously, let y_* be the element in Y_N corresponding to x_* . We use y_* as a proxy for the value of $y(x)$, the mean response at new location x , which is unknown. Next, let $X_n(x_*)$

denote an n -sized neighborhood for predicting at x_* , i.e., the n -nearest points to x_* in X_N , excluding x_* . Using these quantities, and for any neighborhood size n , one may fit $\text{LAGP}_n(x_*; X_n(x_*), Y_n)$, furnishing a prediction for y_* . Specifically, let $\mu_n(x_*)$ denote the predictive mean of x_* calculated with neighborhood size n . Suppose we do this for each n of interest, and take the best one by squared error:

$$\hat{n}(x_*) = \arg \min_{n \in \{n_{\min}, \dots, n_{\max}\}} \text{SE}(y_*, \mu_n(x_*)). \quad (5)$$

This $\hat{n}(x_*)$ is the best neighborhood size for x_* , which is nearby the location of interest x . What remains is to refit the local model at x using the $\hat{n}(x_*)$ -nearest neighbors to x , $\text{LAGP}_{\hat{n}(x_*)}(x; X_{\hat{n}(x_*)}(x), Y_{\hat{n}(x_*)})$.

Without care, fitting $(n_{\max} - n_{\min})$ -many GPs in pursuit of Eq. (5) could be prohibitively expensive. One option is parallelization, since the calculation for each n is computationally exclusive of the others. However, we prefer to parallelize instead over the predictive location(s), $x \in \mathcal{X}$, which will be described in Section 5. A computationally thrifty solution takes advantage of the nested structure of neighborhoods as n increases: $X_{n_{\min}}(x_*) \subseteq X_{n_{\min}+1}(x_*) \subseteq \dots \subseteq X_{n_{\max}}(x_*)$. Observe that any two neighborhoods $X_n(x_*)$ and $X_{n-1}(x_*)$ are identical except for one point: the n^{th} furthest point from x_* . Let $x_n = X_n(x_*) \setminus X_{n-1}(x_*)$ denote this new location as the neighborhood increases by one. A visual of these x_n , selected from X_N on a 25×25 grid, is provided in the left panel of Figure 4. Each number indicates the position of x_n for some

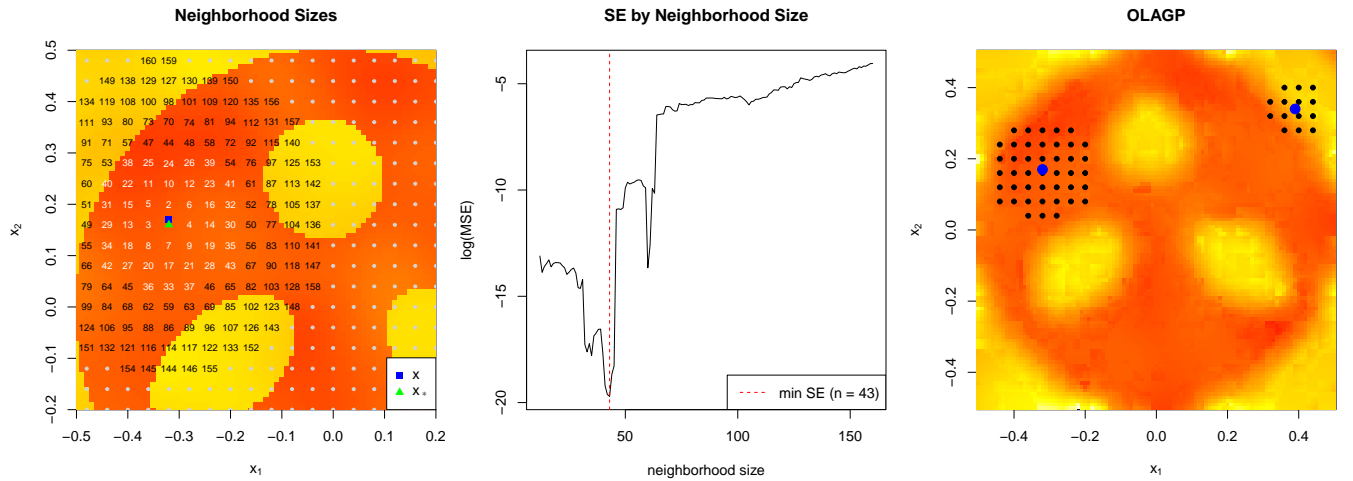


Figure 4: *Left*: Order of LAGP neighborhood for point $(-0.32, 0.17)$; *Center*: SE by neighborhood size for point $(-0.32, 0.17)$; *Right*: Optimal neighbors LAGP (OLAGP) fit. Blue dots indicate two predictive sites and the surrounding black dots are the respective optimal neighborhoods.

n relative to $x_* \in X_N$, the closest point to $x = (-0.32, 0.17)$.

Now, proceeding in order for $n = n_{\min}, \dots, n_{\max}$, suppose we had already calculated $\text{LAGP}_{n-1}(x_*)$, beginning initially with $n-1 \equiv n_{\min}$ via the description in Section 2.2, yielding $\Sigma_{n-1}^{-1} \equiv \Sigma(X_{n-1}(x_*))^{-1}$ and similarly for $\log |\Sigma_{n-1}|$. Incorporating the next point, x_n , involves adding a new row/column to Σ_{n-1} to get Σ_n , which may be calculated without new cubic cost matrix decompositions by following the partition inverse equations (Barnett, 1979). Specifically,

$$\Sigma_n^{-1} = \begin{bmatrix} [\Sigma_{n-1}^{-1} + hh^\top v] & h \\ h^\top & v^{-1} \end{bmatrix} \quad \text{and} \quad \log |\Sigma_n| = \log |\Sigma_{n-1}| + \log(v), \quad \text{where} \quad (6)$$

$$h = -v^{-1} \Sigma_{n-1}^{-1} \Sigma(X_{n-1}(x_*), x_n), \quad \text{and} \quad v = \Sigma(x_n) - \Sigma(x_n, X_{n-1}(x_*)) \Sigma_{n-1}^{-1} \Sigma(X_{n-1}(x_*), x_n).$$

Each update is quadratic in n , so that the entire process requires $c \sum_n^{n_{\max}} n^2 \in \mathcal{O}(n_{\max}^3)$ flops. In other words, the computational expense is no greater than that involved in computing the largest LAGP in the search. Given these quantities, $\mu_n(x_*)$ required as in Eq. (4) is again at worst cubic in n .

These updates, and the computational cost analysis, presume that Σ_{n-1} and Σ_n utilize the same hyperparameters, like lengthscales θ_k , which may not be ideal. In particular, shorter lengthscales will generally be preferred for smaller n_{\min} -sized neighborhoods whose squared distances (3) are short. Whereas when n is closer to n_{\max} , including longer squared distances, longer lengthscales may be preferred. However, an MLE calculation (2) after each update, as new x_n arrives, would incur cubic costs and result in a quartic overall computational complexity, which is not ideal either. Recognizing that an additional data point is of greater value to the likelihood, say via its Fisher information, when n is small as opposed to large, we deploy a logarithmic MLE-updating schedule so that cubic MLE costs are incurred much less often as n increases. Any sub-linear updating schedule will keep computation cubic. The details, summarizing the

Algorithm 1 OLAGP (Optimal Neighbors LAGP)

Require: $X_N, Y_N, x, n_{\min}, n_{\max}$

- 1: $x_* = X_1(x)$ ▷ nearest neighbor of x
 - 2: $\{\Sigma_{n_{\min}}^{-1}, \log |\Sigma_{n_{\min}}|\} = \text{chol}(\Sigma(X_{n_{\min}}(x_*)))$ ▷ calculate $\Sigma_{n_{\min}}^{-1}$ and $\log |\Sigma_{n_{\min}}|$ using (3)
 - 3: $\{\tau^2, \theta\} = \text{MLE}(\Sigma_{n_{\min}}^{-1}, \log |\Sigma_{n_{\min}}|, Y_{n_{\min}})$ ▷ calculate starting MLE using (2)
 - 4: $\mu_{n_{\min}}(x_*) = \Sigma(x_*, X_{n_{\min}}(x_*))\Sigma_{n_{\min}}^{-1}Y_{n_{\min}}$ ▷ make prediction for x_* using (4)
 - 5: **for** $n \in \{n_{\min} + 1, \dots, n_{\max}\}$ **do**
 - 6: $x_n = X_n(x_*) \setminus X_{n-1}(x_*)$ ▷ newest point in neighborhood
 - 7: $\{\Sigma_n^{-1}, \log |\Sigma_n|\} = \text{update}(\Sigma_{n-1}^{-1}, \log |\Sigma_{n-1}|, x_n)$ ▷ calculate new Σ_n^{-1} and $|\Sigma_n|$ using (6)
 - 8: **if** $\log_2(n) \bmod 1 = 0$ **then**
 - 9: $\{\tau^2, \theta\} = \text{MLE}(\Sigma_n^{-1}, \log |\Sigma_n|, Y_n)$ ▷ recalculate MLE using (2)
 - 10: **end if**
 - 11: $\mu_n(x_*) = \Sigma(x_*, X_n(x_*))\Sigma_n^{-1}Y_n$ ▷ make prediction for x_* using (4)
 - 12: **end for**
 - 13: $\hat{n}(x_*) = \underset{n \in \{n_{\min}, \dots, n_{\max}\}}{\text{argmin}} \text{SE}(y_*, \mu_n(x_*))$ ▷ choose best neighborhood size using (5)
 - 14: **return** $\text{LAGP}_{\hat{n}(x_*)}(x; X_{\hat{n}}(x), Y_{\hat{n}})$ ▷ make prediction for x with $\hat{n}(x_*)$
-

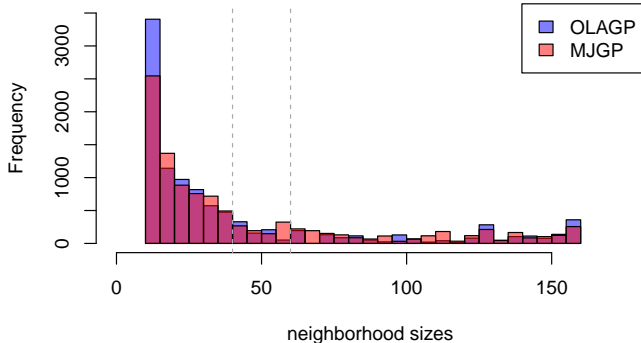
entirety of our approach to solving Eq. (5), is provided by Algorithm 1. Notice that the procedure ends after re-fitting LAGP with the chosen $\hat{n}(x_*)$ with x and all of X_N .

Continuing our illustration in Figure 4, the center panel provides a view of the SE-values encountered via Eq. (5) using the setup on the left, for $x = (-0.32, 0.17)$, as n ranges from $n_{\min} = 12$ to $n_{\max} = 160$. The result is $\hat{n}(x) = 43$, and the indices for these locations are indicated with white text. Notice how $\hat{n}(x)$ is chosen such that $X_{\hat{n}}(x)$ is as big as possible while residing entirely in the red-response area. This process must be repeated for $x \in \mathcal{X}$ of interest, whereas only one is illustrated in the figure. Some of the details of how we recommend doing this are deferred to Section 5. A **for** loop around Algorithm 1 is one simple option, and is the basis of the illustration described next.

3.2 An Illustration

Now consider applying Alg. 1 independently on each $x \in \mathcal{X}$, e.g., testing on a 101×101 grid, extending our running ‘‘Phantom’’ example. The right panel of Figure 4 uses color to indicate the predictive means obtained at each x on the last line of the algorithm. Compared to the truth [Figure 3] the fit looks good, but not perfect. We show in Appendix B.1 that this fit is more accurate by root mean square prediction

error (RMSPE) than an ordinary GP fit. Here we aim to illustrate the optimal choice of neighborhood size, $\hat{n}(x)$, in two ways. We begin with focus on two particular predictive locations: $(-0.32, 0.17)$ and $(0.39, 0.34)$, far from and near to the manifold of discontinuity, respectively. Observe how the optimal neighborhood size (OLAGP) adjusts as appropriate ($n = 43$ far from the manifold; $n = 14$ near).



Size	OLAGP	MJGP
12–20	4548	3914
21–40	2838	2853
41–60	745	933
61–80	414	697
81–100	319	298
101–120	139	396
121–140	511	544
141–160	687	566

Figure 5: Distribution of OLAGP and MJGP [Section 4] estimated neighborhood sizes.

Now consider how all 10,201 neighborhoods, over the whole grid \mathcal{X} , compare to the `laGP` software default of $n = 50$. Figure 5 shows how that choice (between the vertical lines) is not advantageous for the Phantom data. Many smaller, but also many much larger neighborhoods are estimated by OLAGP, and with much greater frequency. The figure also provides neighborhoods for the new method (“MJGP”) discussed next in Section 4.

Before turning to that, we note anecdotally that OLAGP performs worst at or near the manifold of discontinuity (See Appendix B.1). This is because it cannot choose $\hat{n}(x)$ small enough to exclude points from the opposite side of the manifold without maintaining a viable minimum ($n_{\min} = 12$) for a GP fit. Observe how the neighborhood for $(0.39, 0.34)$ contains several points in the red region. At $\hat{n}(x) = 14$ for that location, the neighborhood cannot shrink much further. Consequently, the resulting mean predictions (4) are weighted averages of red- and yellow-region response values. This will yield predictions between 0.4 and 0.6, which we know from Figure 3 are inaccurate. Shrinking neighborhoods farther, even below $n_{\min} = 12$, is a double-edged sword: less data means greater reactivity, but also lower information content. It would be better to allow a more flexible notion of neighborhood, beyond simple Euclidean distance in X_N . Next, we suggest how that can be done without fundamentally altering the LAGP setup by introducing a latent variable. To foreshadow, observe that the “MJGP” neighborhood sizes summarized in Figure 5 show fewer small neighborhoods, *and* fewer large neighborhoods compared to OLAGP.

4 Modular Jump Gaussian Processes

Next we target disparate levels of data from a jump process: first identifying marginally, then predicting spatially, ultimately constructing a feature that can be used as a predictor in a (LA)GP.

4.1 Identifying and predicting levels

Data Y_N from a jump process can often be partitioned marginally (i.e., y without x), which can inform a more complex spatial partition over x . To see this, consider again the histogram of the marginal Y_N for the Phantom data [Figure 3, *right*]. There are two, roughly symmetric, well-separated densities, centered at 0.2 and 0.8. These modes are so well separated you can partition it visually, say at $y = 0.5$.

Visual partitioning of the marginal response will not always be possible, as we shall show momentarily, and it is unsatisfying to require a human in the loop of an otherwise easily automatized procedure. We assume generally that data from jump processes can be captured, marginally, as a mixture distribution with two components. Under this assumption, each observation y_i is associated with a latent variable $\ell_i \in \{1, 2\}$ describing the component y_i belongs to. Of interest to us is the quantity $\mathbb{P}(\ell_i = j)$ for $j = 1, 2$, the probability that observation y_i belongs to component j .

A model-based clustering method can be used to identify the level labels of each observation in Y_N . We prefer EM (Dempster et al., 1977; McLachlan and Krishnan, 1997) under Gaussian mixtures (McLachlan and Basford, 1988, Chapter 2), extracting $\mathbb{P}(\ell_i = j) \equiv \tau_{ji}$ in the notation of that paper. Then, let $c_i = \arg \max_{j \in \{1, 2\}} \mathbb{P}(\ell_i = j)$, the highest probability component for y_i . One view of the results of such a clustering is indicated via the marginal histogram in Figure 3, where color indicates each c_i , $i = 1, \dots, n$; bars colored red are sorted into component 1, yellow into component 2.

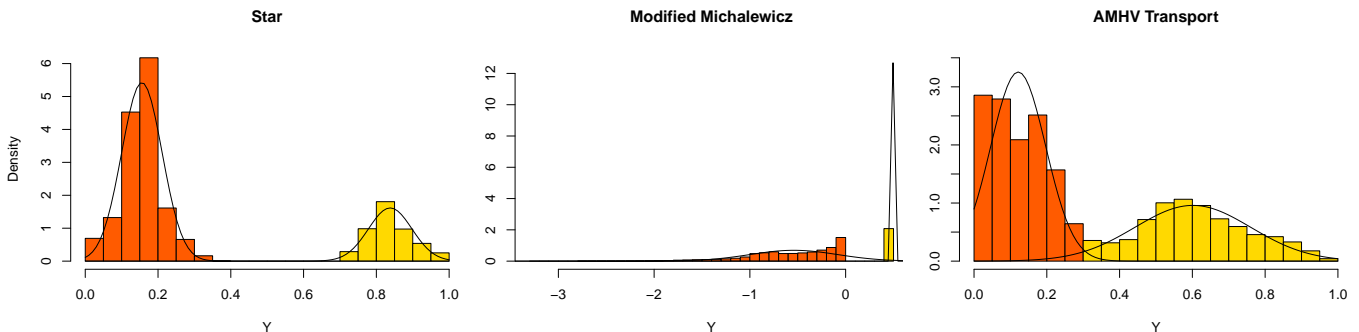


Figure 6: *Left*: Star histogram; *Middle*: Modified Michalewicz function histogram; *Right*: AMHV transport histogram. Colors represent the two levels identified by each clustering algorithm.

Figure 6 provides similar views for three other examples entertained in our empirical work in Section 5, including our motivating real-data set (right panel). In these plots, we also include lines showing the two-component Gaussian mixture estimated by EM. Like the Phantom, the Star example (left panel) is relatively simple. Visual partitioning would have sufficed. The other two benefit from a deliberate, model-based approach. In both of these examples (middle and right panels), it may well be that more than two components (or non-Gaussian ones) would be preferable. However, we aim to show that a crude marginal “partition” is powerful when this information is reincorporated spatially, which we describe next.

Let $c_i \in \{1, 2\}$, $i = 1, \dots, N$ denote the level learned for each $y_i \in Y_N$ via model based clustering, with vector C_N holding all N levels. For example, we could have $c_i = 2$ correspond to “yellow” and 1 for “red”, or vice-versa. Then, pair these with inputs X_N to form (X_N, C_N) , comprising “data” for a spatial classification task. Here we shall write $\hat{f}(\cdot) = \text{class}(X_N, C_N)$, generically, for the predictive equations of a fitted, spatial classification. One option is (basis-expanded) linear logistic regression, or logistic GP classification (e.g Rasmussen and Williams, 2006, Chapter 3). Any classification method works, although the accuracy of a particular method on a particular data set should be tested, for example by evaluating classification accuracy on X_N , before proceeding. Our preferred implementation is detailed in Section 5. We may then use \hat{f} to predict component membership at testing locations \mathcal{X} : $\hat{f}(x) = \mathbb{P}(y(x) = 1)$ for any $x \in \mathcal{X}$. Predicted probabilities for the Phantom data are shown in the left panel of Figure 7 with the manifold of discontinuity overlaid. The other panels will be discussed momentarily, in Section 4.2. Observe how the contours in this plot are similar in shape to the original data [see Figure 3], with values close to 0 in deeply yellow regions and values close to 1 in deeply red regions. In particular, note that $\hat{f}(x) = 0.5$

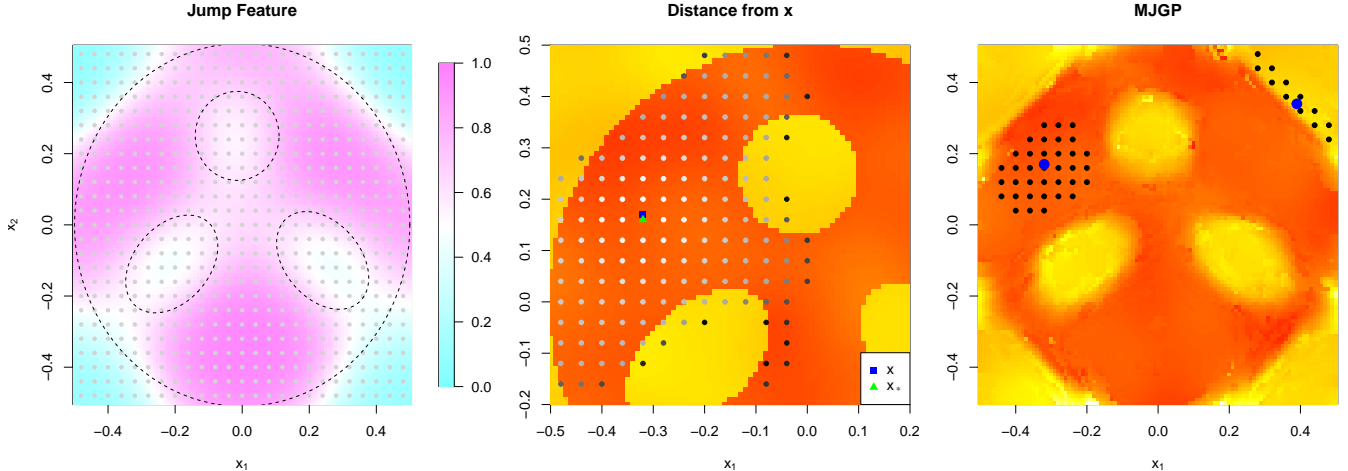


Figure 7: *Left*: Jump feature. *Center*: Nearest 160 neighbors to $x = (-0.32, 0.17)$ after adding the jump feature. White points are closest to x , and black points are furthest away. *Right*: MJGP fit. Blue dots are two predictive locations and the surrounding black dots are the selected neighborhood.

for locations x near the manifold of discontinuity, where component membership is least certain.

4.2 A new feature for GP regression

Now recall that stationary kernels enforce a covariance structure that is based only on the pairwise distances between points (3). As the distance between two points increases, their covariance decreases. This covariance is then used in the GP mean prediction (4), where it serves as a weight. This means that points that are close to the predictive location have a lot of influence on its mean, and points that are far away have little influence. Therefore, if we can find a way to modify the distances between points so that points from the same component are closer together than those from opposite components, this covariance structure would naturally place more influence on points from the same component than those from the opposite one. A simple way to modify these distances without sacrificing the original distance structure is by augmenting with a new input feature (Bornn et al., 2012).

This new variable should be related to component membership. We propose using the probability of component membership [Section 4.1], which should be high for observations likely to be in one component and low for the other. In our example, classifier $\hat{f}(x)$ predicts the probability each location x belongs to the red region; it is large (close to 1) in deeply red regions and small (close to 0) in deeply yellow regions. Suppose we treat those values as a new feature, comprising a new column of X_N for GP modeling. In the new, higher dimensional input space, points in the red region will be closer together than those from the yellow region, and vice versa. Under the likelihood (2) and when predicting (4), points from the same component will have more influence on each other than on points from opposite components.

For this to work, we need to know the probability of component membership for both Y_N and \mathcal{Y} . Section 4.1 provides estimates of C_N , for Y_N , and $\hat{f}(\mathcal{X})$, for \mathcal{Y} . The issue is that C_N is not a probability; it is a vector consisting of 1s and 2s describing the most likely component a point in Y_N belongs to. However, $\hat{f}(\cdot)$ may be used to predict, in-sample, the probability that Y_N belongs to a particular component. Vectors $\hat{f}(X_N)$ and $\hat{f}(\mathcal{X})$ comprise the training and testing jump features for X_N and \mathcal{X} , respectively. These may be appended as new columns $X \equiv [X, \hat{f}(X)]$ and $\mathcal{X} \equiv [\mathcal{X}, \hat{f}(\mathcal{X})]$, overloading the notation somewhat.

To illustrate the effect this new feature has, consider the center plot of Figure 7, again focusing on

$x = (-0.32, 0.17)$ and its nearest neighbor x_* . We also plot the 160 NNs to x , color coded by the rank of their distance from x . The points that are the lightest are closest to x , and those that are the darkest are furthest away. Note that these distances are calculated prior to hyperparameter fitting. Observe first that the neighborhood is no longer circular; it has become oval-shaped to avoid the yellow region. Any points that are in the yellow region are much further away than their 2d distance would suggest. Their colors are darker than nearby points the red region, and thus farther from x .

We generically notate the fitting stage as $\text{GP}([\mathcal{X}, \hat{f}(\mathcal{X})]; [X_N, \hat{f}(X_N)], Y_N)$, where ‘‘GP’’ can stand in for any type (e.g., global, LAGP, OLAGP) depending on the problem at hand. We refer to this method, beginning with the clustering algorithm and ending with the final GP fit, as a ‘‘MJGP’’. Algorithm 2 provides the details for quick reference.

Algorithm 2 Outline of MJGP

Require: X_N, Y_N, \mathcal{X}

- | | |
|---|---|
| 1: $\hat{C}_N = \text{clust}(Y_N)$ | ▷ perform clustering algorithm on marginal Y_N , yielding $C_N \in \{1, 2\}^N$ |
| 2: $\hat{f}(\cdot) = \text{class}(X_N, C_N)$ | ▷ build classifier mapping X_N to C_N , yielding $\hat{f}(x) = \text{Pr}(y(x) = 1)$ |
| 3: $\text{GP}([\mathcal{X}, \hat{f}(\mathcal{X})]; [X_N, \hat{f}(X_N)], Y_N)$ | ▷ fit any GP (e.g. OLAGP) with jump feature |
-

The right panel of Figure 7 provides a MJGP fit on the Phantom data, contrasting with Figure 4. In this case the GP used is an OLAGP, chosen to illustrate the change in neighborhood structure induced by the MJGP. Here, in Figure 7, both neighborhoods are smaller, but are completely contained to the same side of the manifold. MJGP has improved prediction both visually and via RMSPE (see Appendix B.1) over the global GP, LAGP, and OLAGP.

Now return to Figure 5, summarizing all 10,201 $\hat{n}(x)$ for OLAGP and MJGP. Again, the choice of $n = 50$ (the LAGP default) is not particularly advantageous, except for a small percentage of $x \in \mathcal{X}$. Notice that MJGP slightly prefers more mid-range neighborhood sizes than the optimal neighbors GP. In particular, many fewer small $\hat{n}(x)$ are chosen since the neighborhood shape is no longer circular in the original input space (i.e., ignoring the new feature). This facilitates excluding points from the opposite component without resorting to extremely small neighborhood sizes.

Note that while we have thus far chosen examples where the magnitude of the jump is large compared to the overall variability of the data, that is not required to use MJGP. Data sets with large jumps will see the most improvement when compared to regular GP methods, but using MJGP when jumps are small or nonexistent will not lead to overfitting. See examples of MJGP fit to data with small or nonexistent jumps in Figures 19 and 20 in Appendix C. Although the benefit of using MJGP lessens as the size of the jump decreases, it will not compromise results when jumps are not present.

We chose to use the predicted probability of component membership $\hat{f}(X_N)/\hat{f}(\mathcal{X})$ as a new jump feature. However, we could have instead used the predicted component membership to partition the input space into two regions, and fit separate GPs to each region. If these partitions perfectly matched the manifold of discontinuity, this would outperform MJGP. The problem occurs when the manifold of discontinuity is complex, like in the Phantom example. In this case (see Appendix D), the classifier cannot accurately learn the manifold of discontinuity. MJGP improves upon a partitioned GP by using the predicted probability of component membership, which incorporates the uncertainty of the classifier. Accounting for this extra uncertainty in the model ultimately improves prediction over partitioned GPs.

Our MJGP is purposefully generic: clustering, classifying, predicting, and then fitting with a new feature. We mentioned some of the possible choices for each step (e.g. EM, CGP, and OLAGP), but the choice of methods for clustering, classifying, and regression should be tailored to the context of the problem and the data involved. We aim to show that our preferred instance of MJGP is an improvement

on existing methods in the context of surrogate modeling of jump processes from the recent literature.

5 Implementation and empirical benchmarking

Here we present three simulated and one real-world example(s) to demonstrate the effectiveness of OLAGP and MJGP. A summary of each data set/experiment is included in Table 1; we do not list the clustering algorithm because it did not vary between experiments. Input and response ranges are listed prior to any scaling. Details are provided in separate sub-sections to follow. Broadly, for each data set, we conduct a Monte Carlo (MC) experiment which repeatedly randomly partitions the data into 90:10 training and testing sets. In each each repetition, we sample a random subset of 90% of the data set to be used as the training set, and use the remaining 10% as the testing set. The number of MC trials depends on the computational expense implied by the training data set size N , which varies in the experiments. We present five competing methods:

- **Global GP** via `newGPsep` in `1aGP` (Gramacy, 2016), using defaults. This was excluded from the Modified Michalewicz experiment due to size constraints.
- **LAGP** via `aGPsep` in `1aGP` (Gramacy, 2016), with `method = "nn"` and all other defaults.
- **OLAGP** from Section 3 with $n_{\min} = 12$ and $n_{\max} = 160$.
- **Original JGP (OJGP)** via Park (2022)'s MATLAB library using CEM and quadratic boundaries.
- **MJGP** from Section 4 with further details provided in Table 1.

All experiments were completed in R. Code is provided at <https://bitbucket.org/gramacylab/jumpgp>. In this code we provide functions `aGP.optneigh.par()`, `mjgp()`, and `jgp()` to run OLAGP, MJGP, and OJGP, respectively. OLAGP is parallelized over predictive locations $x \in \mathcal{X}$, turning statistical independence into computational exclusivity via `foreach` (Microsoft and Weston, 2022). OJGP leveraged `R.matlab` (Bengtsson, 2022).

Data	N	d	$\mathbf{X}_N \in$	$\mathbf{Y}_N \in$	Classifier	GP Type	Reps
Phantom	10,201	2	$[-0.5, 0.5]^2$	$(-17, 26)$	CGP	OLAGP	100
Star	10,201	2	$[0, 1]^2$	$(-16, 15)$	CGP	OLAGP	100
Mod. Michalewicz	100,000	4	$[0, \pi]^4$	$(-3.25, 0.5)$	RF	OLAGP	30
AMHV Transport	9,503	4	$[50, 400] \times [1, 5] \times [0.25, 5] \times [0.5, 1.5]$	$(100, 517)$	CGP	Global GP	100

Table 1: Implementation summary for each data set/experiment.

For MJGP, we utilize EM-based clustering and either a CGP (Williams and Barber, 1998) or a random forest (RF; Breiman, 2001) for classification via `mclust` (Scrucca et al., 2023), `kernlab` (Karatzoglou et al., 2004) and `randomForest` (Liaw and Wiener, 2002), respectively. We only prefer a RF over a CGP when n is large, for example during the Modified Michalewicz experiment. Again, see Table 1. Model performance is measured out-of-sample using $\text{RMSPE} = (\frac{1}{m} \sum_{x \in \mathcal{X}} (y(x) - \mu(x))^2)^{1/2}$, for which lower is better. Computation times are in Appendix E and prediction interval coverage is in Appendix F.

5.1 Phantom

In Sections 3–4, we assessed model performance (visually and with RMSPE) on the Phantom data for a single train–test partition. The outcome of a full MC experiment is summarized by boxplots in the left panel of Figure 8. For a more granular view, the right panel draws black lines connecting RMSPEs from

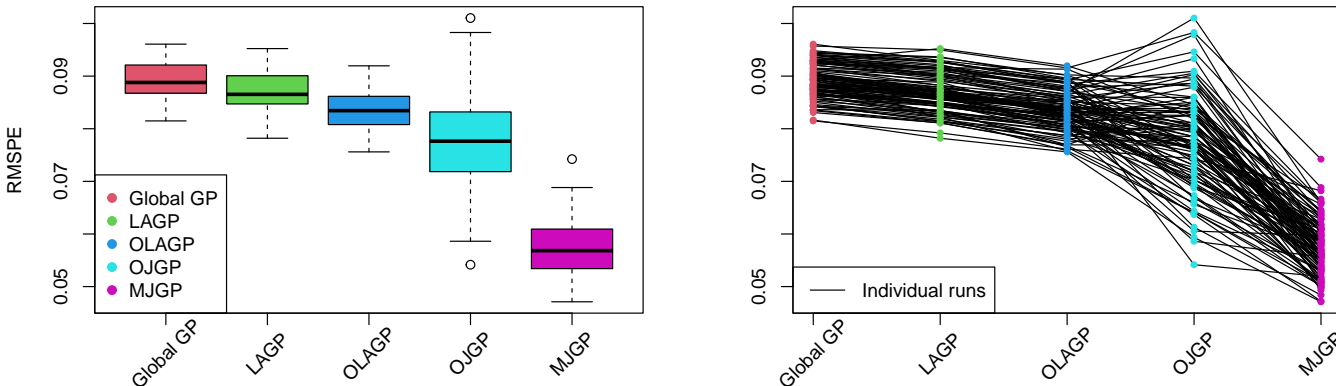


Figure 8: *Left*: MC experiment on the Phantom data set; *Right*: A line plot showing RMSPE at individual runs for each of the five methods. MJGP performs best in all runs.

the same rep, allowing us to see the best performing method for every training/testing set combination. We conclude that most of the overlap of the boxplots is due to variability in the training/testing split. The ordering of accuracy from one MC rep to the next is largely consistent across methods.

In these plots (and all plots in this section), our two methods are shown third from right (OLAGP) and furthest right (MJGP). Both show improvement over the global GP and LAGP, although OLAGP is typically outperformed by OJGP. This is unsurprising, since OJGP was designed specifically for data from jump processes, and OLAGP was not. But notice that MJGP consistently outperforms OJGP, here and broadly over the next few subsections. Looking first at the line plot on the right of Figure 8, we see that for every data set split, predictions made by MJGP are more accurate than those from OJGP. Additionally, the boxplot shows that OJGP has higher variability than MJGP. OJGP makes predictions by estimating a boundary line separating points from the same and opposite components as the predictive location. Our choice of quadratic boundary yields more accurate predictions, but at the expense of higher variability. For more on this distinction, see Park (2022).

5.2 Star

Now consider the “Star” data, which we created for this paper. The goal was to have something like the Phantom, but more angular. Details for how the data set was created are provided in Appendix A.2. See the left panel of Figure 9, with marginal response histogram depicted earlier in the left panel of Figure 6. Like the Phantom, the Star has two well-separated regimes that form a clear shape on the response surface. But the Star is more difficult to model because all points in the yellow regime are geographically close to red ones. It is hard to build a neighborhood inside the yellow portion of the Star.

Repeating themes from the Phantom analysis, consider model performance for a single Star train–test split. Mean fits for the global GP and LAGP are shown in Figure 17 in Appendix B.2, whereas those of OLAGP and MJGP are shown here in the right two panels of Figure 9. RMSPEs can be found in Appendix B.2, where we see that the local methods perform well, with MJGP producing the best predictions of the

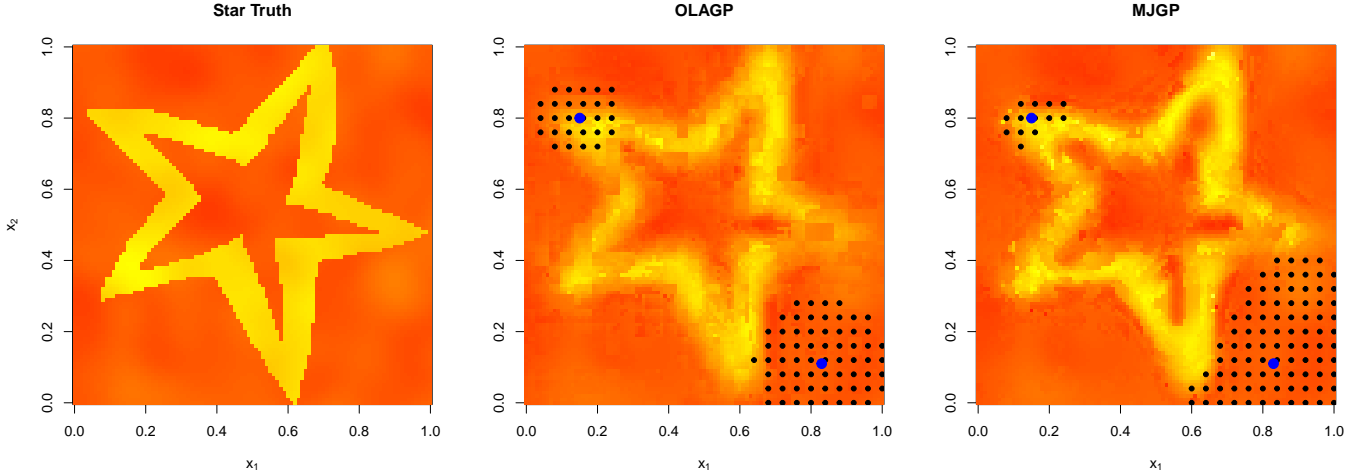


Figure 9: Model fit and chosen neighborhoods for Star data set. *Left*: Ground truth; *Center*: OLAGP fit of Star data set; *Right*: MJGP fit of Star data set. Two predictive locations, in blue, are shown with their chosen neighborhoods, in black.

four. The scenarios depicted in right two panels focus on $x = (0.15, 0.8)$ and $(0.83, 0.11)$. Compared to LAGP, OLAGP has chosen a neighborhood of roughly the same size for $(0.83, 0.11)$, and much smaller for $(0.15, 0.8)$; however, this smaller neighborhood still contains points from the red regime. MJGP provides an interesting change: a much smaller neighborhood size for $(0.15, 0.11)$, and a *larger* neighborhood size for $(0.83, 0.11)$. Both neighborhoods have adapted their shape to only include points from the same regime, and this improves prediction overall.

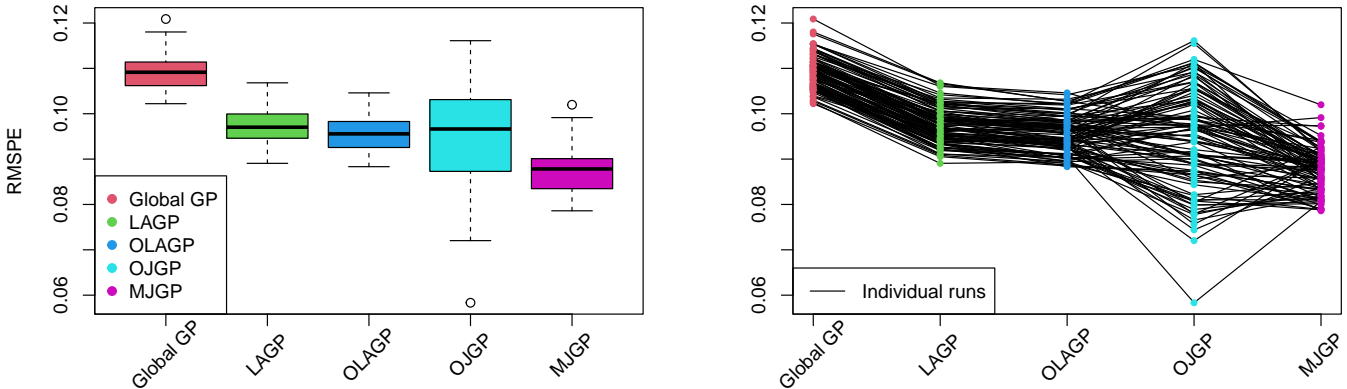


Figure 10: *Left*: MC experiment on the Star data set; *Right*: A line plot showing RMSPE at individual runs for each of the five methods. MJGP performs best in 82 of 100 runs.

Figure 10 summarizes a MC experiment along similar lines. Here again, OLAGP outperforms both the global GP and LAGP; the two JGP methods typically outperform OLAGP. OJGP is again highly variable. Although it outperforms MJGP more frequently than for the Phantom (OJGP was better in 17 of 100 runs), MJGP is still the best performing method for the Star.

5.3 Modified Michalewicz

For a higher-dimensional example, we adapted the so-called Michalewicz function, which can be found in the Virtual Library of Simulation Experiments (Surjanovic and Bingham, 2013). Details can be found in Appendix A.3; note that although the original function is in $[0, \pi]^4$, we scale it to fall in $[0, 1]^4$. Michalewicz is dimension-adaptive; here we present a 4d analysis to match the real data analysis coming in Section 5.4. An LHS design is used with $N = 100,000$ training inputs. The marginal distribution of the response is shown in the center panel of Figure 6. We cannot visualize the response surface in 4d, so instead we show a 2d version in the left panel of Figure 11. Unlike the previous two data sets, the response is not plausibly

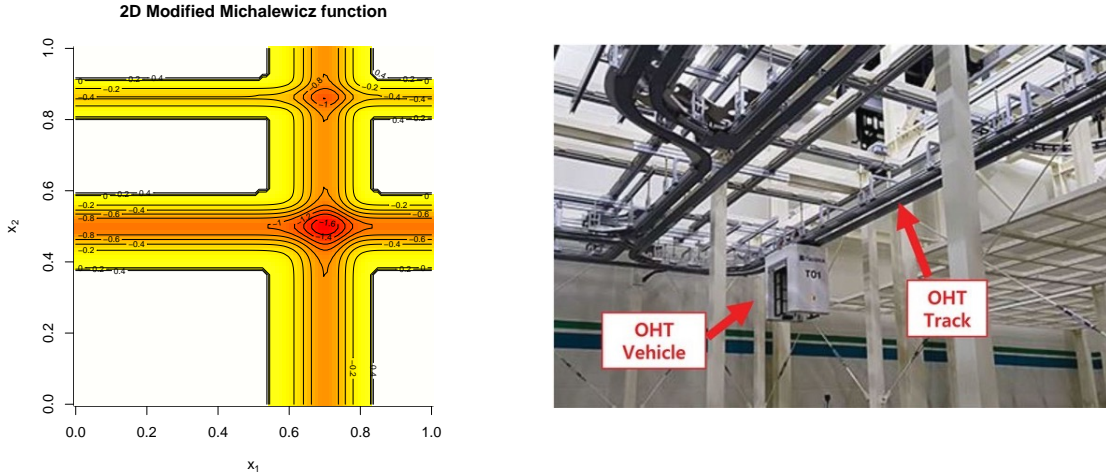


Figure 11: *Left*: Modified Michalewicz response surface in 2d. *Right*: Image of AMHV transport device; taken from Park et al. (2023).

composed of two Gaussian components. Instead, it is comprised of a point mass around 0.5 with other points scattered between in $[-4, 0]$. Nevertheless, we find that EM with two Gaussian components works well in the MJGP setup. One goal of the presentation here is to demonstrate how even a naïve marginal clustering often works well in practice.

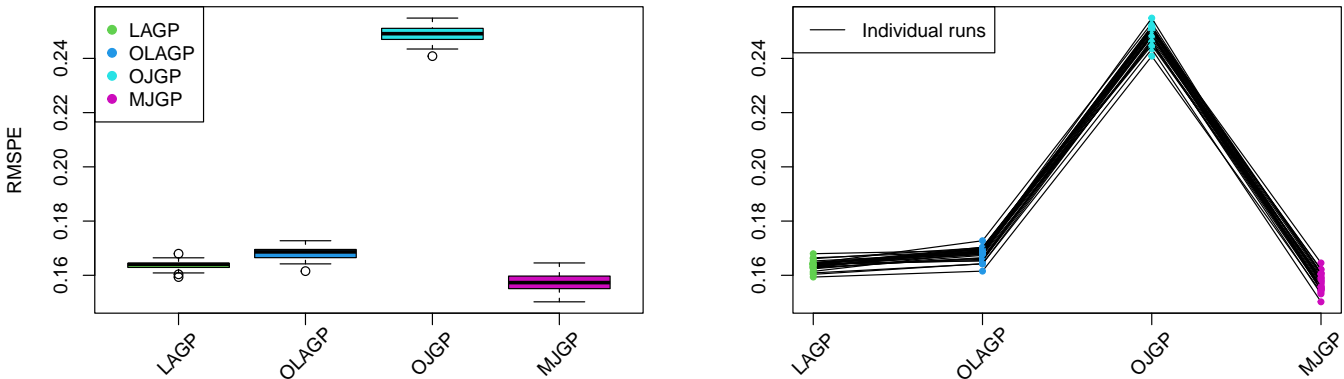


Figure 12: *Left*: MC experiment on the Modified Michalewicz data set; *Right*: A line plot showing RMSPE at individual runs for each of the four methods. MJGP performs best in 29 of 30 runs.

Since N here is very large, we must omit the global GP as a competitor in this experiment. Instead of a CGP we deploy a RF as our classifier. Finally, we limit the number of MC reps to thirty. Results are provided in Figure 12. LAGP, OLAGP, and MJGP all considerably outperform OJGP. LAGP and OLAGP perform comparably, although interestingly LAGP seems to slightly outperform OLAGP in this case. We suspect this is due to the spiky nature of the response surface; see Figure 11. In particular, we believe that OLAGP tends to overestimate the optimal neighborhood size for low values of the response (i.e., the spikes), yielding predictions much higher than the true response. MJGP performs best of all, yielding the lowest RMSPE in 29 of the 30 reps.

5.4 AMHV transport

Finally, consider the AMHV transport data first introduced in Section 1. Specifically, we used a larger version of the data set described in Section 5.2 of Park et al. (2023), scaled so that the inputs lie in the unit hypercube; $d = 4$ and $N = 9,503$. A visual is provided in the right panel of Figure 11. Although N is similar in magnitude to the sample size of the Star and Phantom data sets ($N = 10,201$), the addition of two dimensions means that there is a larger volume to fill. In that sense, this example is the most sparse of the ones entertained in this paper. Outputs are derived from a simulation of the behavior of AMHVs in a particular facility, tallying the average transport time of the AMHVs, including any time spent waiting for the vehicle to arrive. Park et al. (2023) show that as production in the facility increases, transport time, which depends on various design variables, increases and becomes a major bottleneck to the entire manufacturing process. The four variables here include vehicle speed, vehicle acceleration, minimum distance required between vehicles, and the maximum search range of empty vehicles.

A view of the marginal distribution of the response for these data was provided earlier, in the right panel of Figure 6. This is the first example we have looked at where the two clusters overlap. Additionally, the sparse nature of this data set means that local methods do not perform nearly as well. (The closest points in X_N to a predictive location x may actually be far and not representative.) This is a particular problem for OLAGP, which uses x_* as a proxy for x . Consequently, we prefer a global rather than local GP in our application of MJGP for these data.

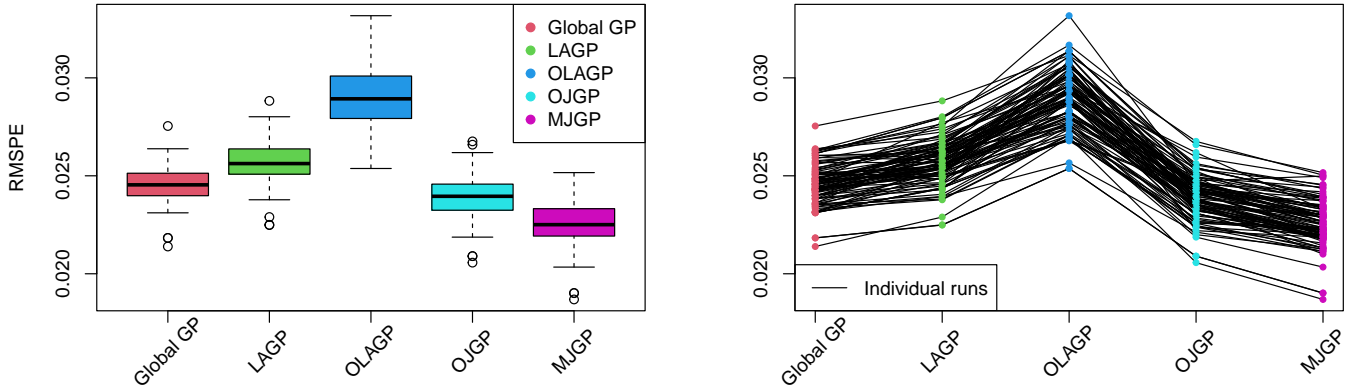


Figure 13: *Left*: MC experiment on the AMHV transport data set; *Right*: A line plot showing RMSPE at individual runs for each of the five methods. MJGP performs best in 99 of 100 runs.

The results of the experiment are shown in Figure 13. As expected, the local methods do not perform as well as the global ones, with OLAGP suffering most. But the global GP performs well, producing

comparable results to OJGP. MJGP produces only slightly better results, but is consistent in doing so (lowest RMSPEs in 99 of the 100 reps).

6 Discussion

We introduced two ideas, adapting LAGP neighborhoods locally (OLAGP) and learning a spatial feature from marginal clustering. Separately, both improve predictions for data from jump processes. They shine brightest when used together. We call this hybrid MJGP, since it involves many of the same ingredients as OJGP, except with off-the-shelf subroutines daisy-chained together.

One opportunity for future work pertains specifically to OLAGP. We mentioned previously that this method has thus far only been implemented for neighborhoods chosen using NN. However, it has been shown that NN neighborhoods can be suboptimal compared to other subdesigns in the GP contexts (Vecchia, 1988; Stein et al., 2004). Gramacy and Apley (2015) demonstrated that neighborhoods chosen via design criteria mean-square prediction error (MSPE) often yield superior LAGP predictions; see their paper for more information on neighborhoods chosen using MSPE. We expect their superior performance to extend to the OLAGP context, but investigating that represents future work.

Other potential opportunities target MJGP more holistically. The first involves extending MJGP to noisy functions. The main concern in this case is whether the signal-to-noise ratio is large enough for the GP to accurately capture jumps in the data. The second involves extending MJGP to allow more than two jump levels. Here we assumed that the marginal response of data from jump processes could be described as a mixture distribution with two components. However, it is possible for the response to have more than two levels. We believe MJGP could be easily extended to this case. The first two steps of clustering and classifying would be very similar to what we described in Section 4. First, cluster Y_N to get $C_N = (c_1, \dots, c_N)^\top$ for $c_i \in \{1, \dots, \ell\}$, where ℓ is the total number of levels. Then use a multiclass classification method – both the CGP from `kernlab` and the RF from `randomForest` have this capability – to fit $\hat{f}(\cdot) = \text{class}(X_N, C_N)$. Extract $\mathbb{P}(y(x) = j)$ for $j = 1, \dots, \ell - 1$. Let $\hat{f}_j(\cdot) = \mathbb{P}(y(x) = j)$ and use each to fit $\text{GP}([\mathcal{X}, \hat{f}_1(\mathcal{X}), \dots, \hat{f}_{\ell-1}(\mathcal{X})]; [X_N, \hat{f}_1(X_N), \dots, \hat{f}_{\ell-1}(X_N)], Y_N)$.

Although we limit our focus to GPs for computer experiments, there is extensive literature connecting GPs and geospatial statistics (Cressie, 1993; Gelfand and Schliep, 2016). Methods exist which fit GPs on errors after accounting for mean structure (Matheron, 1969) or which can account for shifting local mean trends (Haas, 1990). Methods even exist which similarly modify the distance-based kernels according to the covariance between points (Dumelle et al., 2023). Some of these approaches/problems are reminiscent of our jump processes. However, geostatistical methods are typically restricted to 2 or 3 inputs. Computer experiments often contain more input variables.

Acknowledgements

ARF and RBG are grateful for support from NSF 2152679. CP is grateful for support from NSF 2420358. Part of this research was initiated within the frame of the consortium in Applied Mathematics CIROQUO, gathering partners in technological research and academia in the development of advanced methods for Computer Experiments.

Declaration of Interest

The authors report no conflict of interest.

References

- Banerjee, S., Carlin, B., and Gelfand, A. (2004). *Hierarchical Modeling and Analysis for Spatial Data*. Chapman and Hall/CRC.
- Banerjee, S., Gelfand, A. E., Finley, A. O., and Sang, H. (2008). Gaussian predictive process models for large spatial data sets. *Journal of the Royal Statistical Society Series B: Statistical Methodology*, 70(4):825–848.
- Barnett, S. (1979). Matrix methods for engineers and scientists. *McGraw-Hill*.
- Bengtsson, H. (2022). *R.matlab: Read and Write MAT Files and Call MATLAB from Within R*. R package version 3.7.0.
- Bornn, L., Shaddick, G., and Zidek, J. V. (2012). Modeling nonstationary processes through dimension expansion. *Journal of the American Statistical Association*, 107(497):281–289.
- Breiman, L. (2001). Random forests. *Machine learning*, 45:5–32.
- Cole, D. A., Christianson, R. B., and Gramacy, R. B. (2021). Locally induced Gaussian processes for large-scale simulation experiments. *Statistics and Computing*, 31(3):33.
- Cressie, N. (1993). *Statistics for spatial data (Revised edition)*. Wiley: Hoboken, NJ.
- Damianou, A. and Lawrence, N. (2013). Deep Gaussian processes. In *Artificial Intelligence and Statistics*, pages 207–215.
- Datta, A., Banerjee, S., Finley, A. O., and Gelfand, A. E. (2016a). Hierarchical nearest-neighbor Gaussian process models for large geostatistical datasets. *Journal of the American Statistical Association*, 111(514):800–812.
- Datta, A., Banerjee, S., Finley, A. O., and Gelfand, A. E. (2016b). On nearest-neighbor Gaussian process models for massive spatial data. *Wiley Interdisciplinary Reviews: Computational Statistics*, 8(5):162–171.
- Dempster, A. P., Laird, N. M., and Rubin, D. B. (1977). Maximum likelihood from incomplete data via the EM algorithm. *Journal of the royal statistical society: series B (methodological)*, 39(1):1–22.
- Dumelle, M., Higham, M., and Ver Hoef, J. M. (2023). spmodel: Spatial statistical modeling and prediction in R. *PLoS One*, 18(3):e0282524.
- Garnett, R., Osborne, M. A., Reece, S., Rogers, A., and Roberts, S. J. (2010). Sequential Bayesian prediction in the presence of changepoints and faults. *The Computer Journal*, 53(9):1430–1446.
- Gelfand, A. E. and Schliep, E. M. (2016). Spatial statistics and Gaussian processes: A beautiful marriage. *Spatial Statistics*, 18:86–104.
- Gramacy, R., Niemi, J., and Weiss, R. (2014). Massively parallel approximate Gaussian process regression. *SIAM/ASA Journal on Uncertainty Quantification*, 2(1):564–584.
- Gramacy, R. B. (2016). laGP: large-scale spatial modeling via local approximate Gaussian processes in R. *Journal of Statistical Software*, 72:1–46.

- Gramacy, R. B. (2020). *Surrogates: Gaussian process modeling, design, and optimization for the applied sciences*. CRC press.
- Gramacy, R. B. and Apley, D. W. (2015). Local Gaussian process approximation for large computer experiments. *Journal of Computational and Graphical Statistics*, 24(2):561–578.
- Gramacy, R. B. and Haaland, B. (2016). Speeding up neighborhood search in local Gaussian process prediction. *Technometrics*, 58(3):294–303.
- Gramacy, R. B. and Lee, H. K. H. (2008). Bayesian treed Gaussian process models with an application to computer modeling. *Journal of the American Statistical Association*, 103(483):1119–1130.
- Haas, T. C. (1990). Lognormal and moving window methods of estimating acid deposition. *Journal of the American Statistical Association*, 85(412):950–963.
- Karatzoglou, A., Smola, A., Hornik, K., and Zeileis, A. (2004). kernlab—an S4 package for kernel methods in R. *Journal of statistical software*, 11:1–20.
- Kaufman, C. G., Bingham, D., Habib, S., Heitmann, K., and Frieman, J. A. (2011). Efficient emulators of computer experiments using compactly supported correlation functions, with an application to cosmology.
- Kim, H.-M., Mallick, B. K., and Holmes, C. C. (2005). Analyzing nonstationary spatial data using piecewise Gaussian processes. *Journal of the American Statistical Association*, 100(470):653–668.
- Liaw, A. and Wiener, M. (2002). Classification and regression by randomForest. *R News*, 2(3):18–22.
- Luo, Z. T., Sang, H., and Mallick, B. (2023). A nonstationary soft partitioned Gaussian process model via random spanning trees. *Journal of the American Statistical Association*, pages 1–12.
- Matheron, G. (1969). *Le krigeage universel*, volume 1. École nationale supérieure des mines de Paris Paris.
- McKay, M. D., Beckman, R. J., and Conover, W. J. (1979). A comparison of three methods for selecting values of input variables in the analysis of output from a computer code. *Technometrics*, 21(2):239–245.
- McLachlan, G. J. and Basford, K. E. (1988). *Mixture models: Inference and applications to clustering*, volume 38. M. Dekker New York.
- McLachlan, G. J. and Krishnan, T. (1997). *The EM algorithm and extensions*. John Wiley & Sons.
- Microsoft and Weston, S. (2022). *foreach: Provides Foreach Looping Construct*. R package version 1.5.2.
- Nychka, D., Bandyopadhyay, S., Hammerling, D., Lindgren, F., and Sain, S. (2015). A multiresolution Gaussian process model for the analysis of large spatial datasets. *Journal of Computational and Graphical Statistics*, 24(2):579–599.
- Park, C. (2022). Jump Gaussian process model for estimating piecewise continuous regression functions. *The Journal of Machine Learning Research*, 23(1):12737–12773.
- Park, C., Qiu, P., Carpena-Núñez, J., Rao, R., Susner, M., and Maruyama, B. (2022). Sequential adaptive design for jump regression estimation. *IISE Transactions*, 55(2):111–128.

- Park, C., Waelder, R., Kang, B., Maruyama, B., Hong, S., and Gramacy, R. (2023). Active learning of piecewise Gaussian process surrogates. *arXiv preprint arXiv:2301.08789*.
- Payne, R. D., Guha, N., Ding, Y., and Mallick, B. K. (2020). A conditional density estimation partition model using logistic Gaussian processes. *Biometrika*, 107(1):173–190.
- Picheny, V., Vakili, S., and Artemev, A. (2019). Ordinal bayesian optimisation. *arXiv preprint arXiv:1912.02493*.
- Pope, C. A., Gosling, J. P., Barber, S., Johnson, J. S., Yamaguchi, T., Feingold, G., and Blackwell, P. G. (2021). Gaussian process modeling of heterogeneity and discontinuities using Voronoi tessellations. *Technometrics*, 63(1):53–63.
- Rasmussen, C. E. and Williams, C. K. (2006). *Gaussian processes for machine learning*, volume 2. MIT press Cambridge, MA.
- Sacks, J., Welch, W., Mitchell, T., and Wynn, H. (1989). Design and analysis of computer experiments. *Statistical Science*, 4(4):409–423.
- Sampson, P. and Guttorp, P. (1992). Nonparametric estimation of nonstationary spatial covariance structure. *Journal of the American Statistical Association*, 87(417):108–119.
- Santner, T. J., Williams, B. J., Notz, W. I., and Williams, B. J. (2003). *The design and analysis of computer experiments*, volume 1. Springer.
- Sauer, A., Cooper, A., and Gramacy, R. B. (2023a). Non-stationary Gaussian process surrogates. *arXiv preprint arXiv:2305.19242*.
- Sauer, A., Cooper, A., and Gramacy, R. B. (2023b). Vecchia-approximated deep Gaussian processes for computer experiments. *Journal of Computational and Graphical Statistics*, 32(3):824–837.
- Schabenberger, O. and Gotway, C. A. (2017). *Statistical methods for spatial data analysis*. Chapman and Hall/CRC.
- Schmidt, A. and O’Hagan, A. (2003). Bayesian inference for non-stationary spatial covariance structure via spatial deformations. *Journal of the Royal Statistical Society: Series B (Statistical Methodology)*, 65(3):743–758.
- Scrucca, L., Fraley, C., Murphy, T. B., and Raftery, A. E. (2023). *Model-Based Clustering, Classification, and Density Estimation Using mclust in R*. Chapman and Hall/CRC.
- Snelson, E. and Ghahramani, Z. (2005). Sparse gaussian processes using pseudo-inputs. *Advances in neural information processing systems*, 18.
- Stein, M. L. (2012). *Interpolation of spatial data: some theory for kriging*. Springer Science & Business Media.
- Stein, M. L., Chi, Z., and Welty, L. J. (2004). Approximating likelihoods for large spatial data sets. *Journal of the Royal Statistical Society Series B: Statistical Methodology*, 66(2):275–296.
- Sung, C.-L., Gramacy, R. B., and Haaland, B. (2018). Exploiting variance reduction potential in local Gaussian process search. *Statistica Sinica*, pages 577–600.

- Surjanovic, S. and Bingham, D. (2013). Virtual library of simulation experiments: Test functions and datasets. Retrieved February 1, 2024, from <http://www.sfu.ca/~ssurjano>.
- Toms, J. D. and Lesperance, M. L. (2003). Piecewise regression: a tool for identifying ecological thresholds. *Ecology*, 84(8):2034–2041.
- Vecchia, A. V. (1988). Estimation and model identification for continuous spatial processes. *Journal of the Royal Statistical Society Series B: Statistical Methodology*, 50(2):297–312.
- Vieth, E. (1989). Fitting piecewise linear regression functions to biological responses. *Journal of Applied Physiology*, 67(1):390–396.
- Williams, C. K. and Barber, D. (1998). Bayesian classification with Gaussian processes. *IEEE Transactions on Pattern Analysis and Machine Intelligence*, 20(12):1342–1351.
- Zimmerman, D. L. and Ver Hoef, J. M. (2024). *Spatial linear models for environmental data*. Chapman and Hall/CRC.

SUPPLEMENTARY MATERIAL

A Data Generation Details

Here we describe the process for generating the Phantom, Star, and Modified Michalewicz data sets.

A.1 Phantom

The Phantom data set is generated in the same way as the Phantom data set in Park (2022), but with different hyperparameter values. This version of the Phantom is evaluated on an evenly spaced 101×101 grid in $[-0.5, 0.5]^2$. The response is generated using the partitioning scheme shown in the left panel of Figure 14. In this plot, the color represents the true component membership of every input combination: white pixels belong to component 1, and black pixels belong to component 2. Data are drawn from a $\mathcal{N}_{N_i}(\mu_i, \Sigma(X_{N_i}))$, where N_i is the number of observations in component i , μ_i is the mean of component i , and X_{N_i} is the subset of observations which belong to component i . The mean vector is $\mu = [27, 0]^\top$ and the covariance matrix $\Sigma(X_{N_i})$ is calculated using the exponential covariance function (3) with $\tau^2 = 9$ and $\theta = [0.1, 0.1]^\top$. After sampling all the data, the response was standardized so that $Y_N \in [0, 1]$.

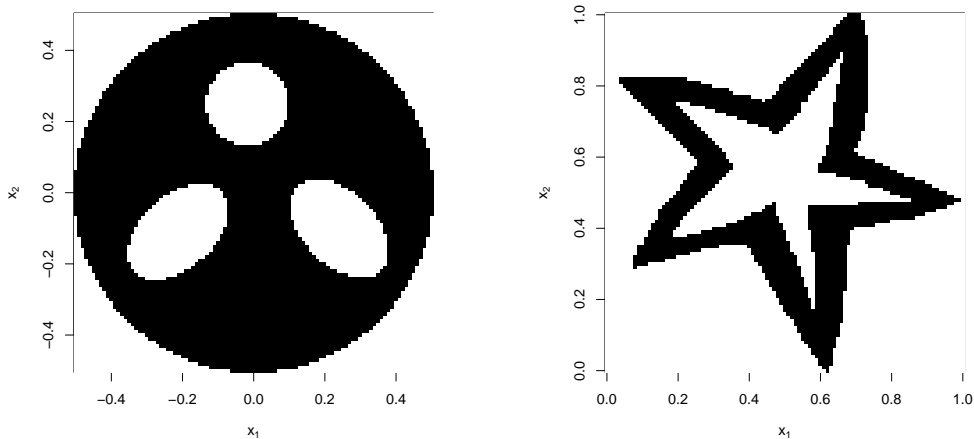


Figure 14: *Left*: Image describing component membership for Phantom data set; *Right*: Image describing component membership for Star data set.

A.2 Star

The Star data set is inspired by the Star data set in Park (2022), but uses a different image for its partitioning structure. This version of the Star is evaluated on an evenly spaced 101×101 grid in $[0, 1]^2$. The response is generated using the partitioning scheme shown in the right panel of Figure 14. Like with the Phantom, the color represents the true component membership: white for component 1, and black for component 2. Data are drawn from a $\mathcal{N}_{N_i}(\mu_i, \Sigma(X_{N_i}))$. The mean vector is $\mu = [-10, 10]^\top$ and the covariance matrix $\Sigma(X_{N_i})$ is calculated using the exponential covariance function (3) with $\tau^2 = 3$ and $\theta = [0.01, 0.01]^\top$. After sampling all the data, the response was standardized so that $Y_N \in [0, 1]$.

A.3 Modified Michalewicz

The Modified Michalewicz is a modification of the Michalewicz function from the Virtual Library of Simulation Experiments (Surjanovic and Bingham, 2013). The original Michalewicz function is defined as $f(x) = -\sum_{i=1}^d \sin(x_i) \sin^{2m}\left(\frac{ix_i^2}{\pi}\right)$ for $x \in [0, \pi]^4$ and d in arbitrary dimension. We use $d = 4$ and $m = 10$ (the recommended default) with inputs coded into $[0, 1]^4$. We first evaluate $f(x)$ using an LHS of size 100,000. The Modified Michalewicz is then defined as:

$$y(x) = \begin{cases} f(x) & f(x) \leq -0.01 \\ f(x) + 0.5 & f(x) > -0.01. \end{cases} \quad (7)$$

We use this modification because the response surface of $f(x)$, without modifications, contains no jumps. It is comprised of many local minima that are surrounded by a nearly flat surface around 0. Consequently, the marginal response is comprised of two “levels”: a point mass around 0, and the rest of the surface. To create the jumps (i.e. discontinuities) that we expect, we raise the flat area of the surface by 0.5. This creates a manifold of discontinuity where the response jumps from the point mass to the rest of the surface.

B Global and LAGP Fits

We provide the mean fits given by a global GP and LAGP for the Phantom and Star data sets to highlight the improvements made by OLAGP and MJGP. We also provide the difference between the predicted mean fit and the truth for each data set.

B.1 Phantom

The left two panels of Figure 15 show the predicted mean fits for the Phantom data set using global GP and LAGP models. Both fits are visually less accurate than the OLAGP fit in Figure 4 and MJGP fit

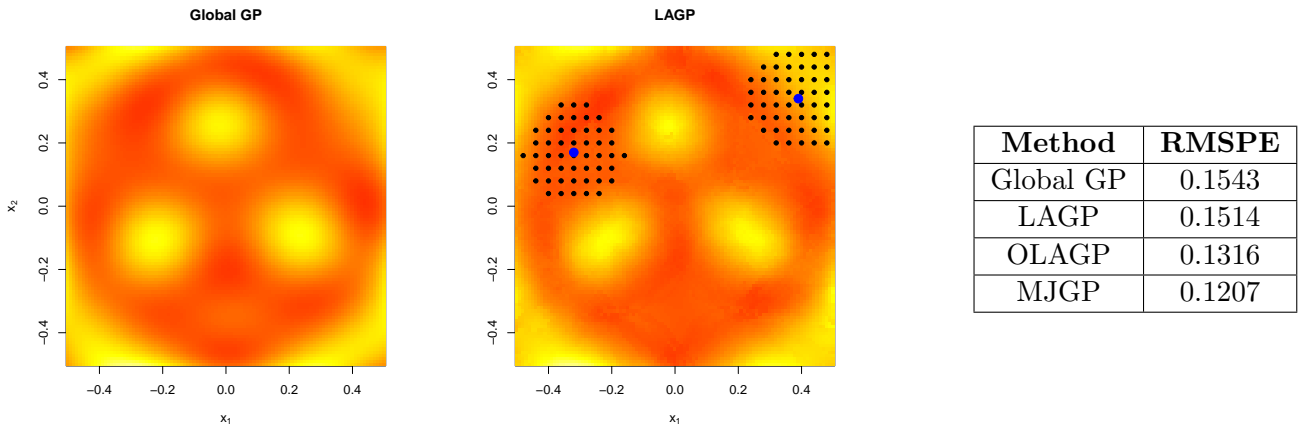


Figure 15: *Left*: Global GP fit. *Center*: LAGP fit. The blue dots are two predictive locations and the surrounding black dots are the selected neighborhood for that predictive location. *Right*: RMSPE of global GP, LAGP, OLAGP, and MJGP fits.

in Figure 7. This is verified by the table of RMSPE values in the right panel, which shows that both OLAGP and MJGP produce more accurate predictions than either method. The LAGP fit in the center

panel also shows the selected neighborhoods for the same two predictive locations used in Sections 3 and 4, $(-0.32, 0.17)$ and $(0.39, 0.34)$. Notice in particular that the neighborhood for $(0.39, 0.34)$ contains points in both the red and yellow regions, which explains why our prediction is inaccurate. We are able to select smaller and differently shaped neighborhoods using OLAGP and MJGP so that our predictions are more accurate. We can verify that OLAGP and MJGP make more accurate predictions by looking at Figure 16, which shows the absolute difference between the mean predictions and the truth. Notice that the difference

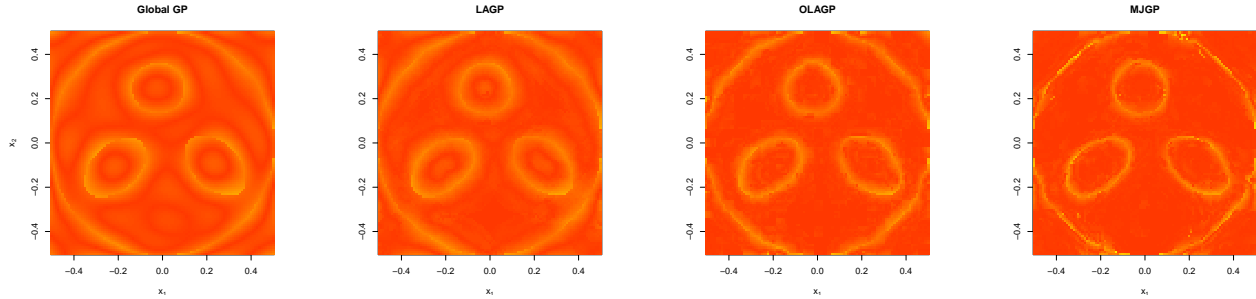


Figure 16: *Left*: Difference between global GP fit and truth; *Center Left*: Difference between LAGP fit and truth; *Center Right*: Difference between OLAGP fit and truth; *Right*: Difference between MJGP fit and truth.

is largest along the manifold of discontinuity.

B.2 Star

The left two panels of Figure 17 show the predicted mean fits for the Star data set using global GP and LAGP models. Both fits are visually less accurate than the OLAGP and MJGP fits in Figure 9. The global

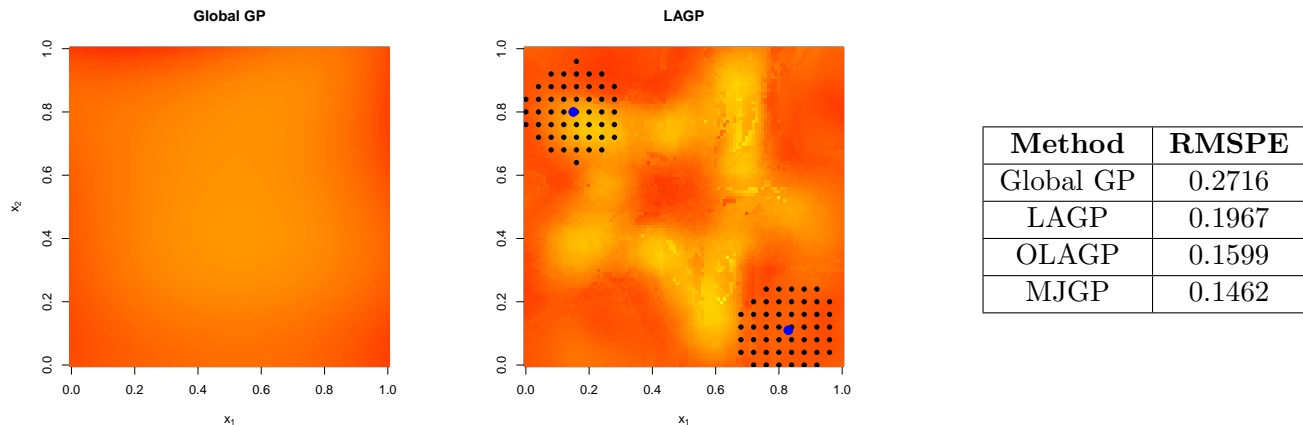


Figure 17: *Left*: Global GP fit. *Center*: LAGP fit. The blue dots are two predictive locations and the surrounding black dots are the selected neighborhood for that predictive location. *Right*: RMSPE of global GP, LAGP, OLAGP, and MJGP fits.

GP performs particularly bad in this case, likely because the proportion of observations in component 1 is much larger than the proportion of values in component 2. The table of RMSPE values in the right panel verifies our intuition, showing that OLAGP and MJGP produce more accurate predictions than either method, particularly the global GP. The LAGP fit in the center panel also shows the selected neighborhoods

for the same two predictive locations used in Section 5.2, $(0.15, 0.8)$ and $(0.83, 0.11)$. Notice in particular that the neighborhood for $(0.15, 0.8)$ contains points in both the red and yellow regions, which is why our prediction is inaccurate. We are able to select smaller and differently shaped neighborhoods using OLAGP and MJGP so that our predictions are more accurate. We can verify that OLAGP and MJGP make more accurate predictions by looking at Figure 18, which shows the absolute difference between the mean predictions and the truth. Notice that the difference is largest along the manifold of discontinuity.

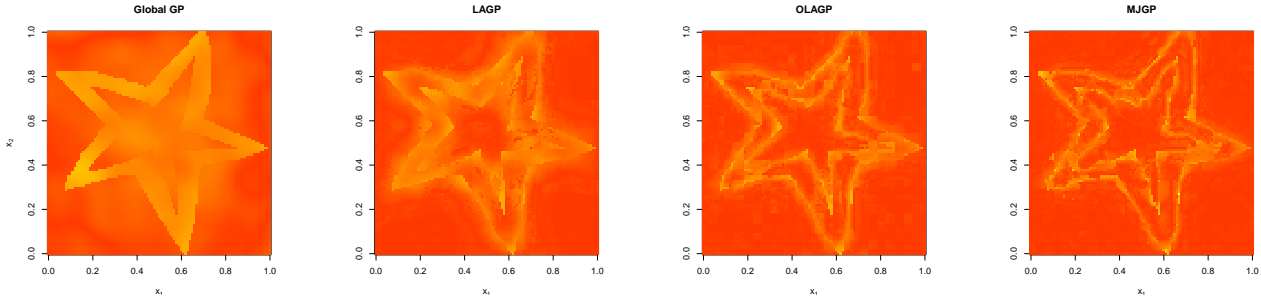


Figure 18: *Left*: Difference between global GP fit and truth; *Center Left*: Difference between LAGP fit and truth; *Center Right*: Difference between OLAGP fit and truth; *Right*: Difference between MJGP fit and truth.

C MJGP – Special Cases

Here we show the performance of MJGP on two special cases – data with small jumps and data with no jumps.

C.1 Data with Small Jumps

For the case with small jumps, we modify the function used in Section 1. We define the same jumping sine curve, but this time with a jump of 2 instead of 10. In other words, we use the function in Eq. 1, but replace the 10 with a 2. We consider modeling this function using three of the four methods in Figure 1; we exclude MJGP with a global GP. The results are shown in Figure 19. The black lines represent the

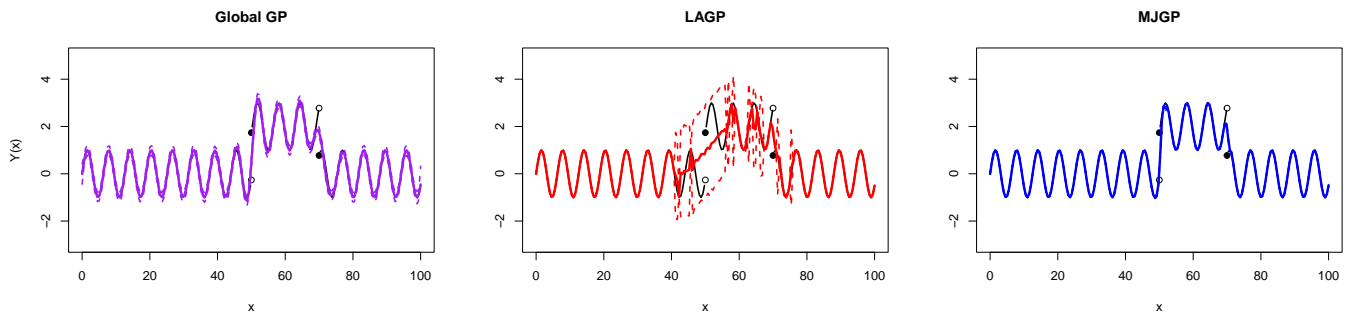


Figure 19: Predictive mean and 95% PI for the small jump case using a (*left*) global GP, (*center*) LAGP, and (*right*) MJGP.

true function, while the colors (purple, red, and blue) represent the predictive mean and 95% PI. We see that MJGP is still able to accurately capture the jumps, and offers improvement over the global GP and

LAGP methods. Calculating RMSPE for each method confirms our findings; the global GP, LAGP, and MJGP produce RMSPEs of 0.1327, 0.4139, and 0.1038, respectively.

C.2 Data with No Jumps

For the case with no jumps, we use a sine curve defined on the same range as our previous functions (i.e., $x \in [0, 100]$) to test MJGP. We use the same three methods for comparison as in the previous section. The results are shown in Figure 20. Here we see that the results do not look much different for any of the three

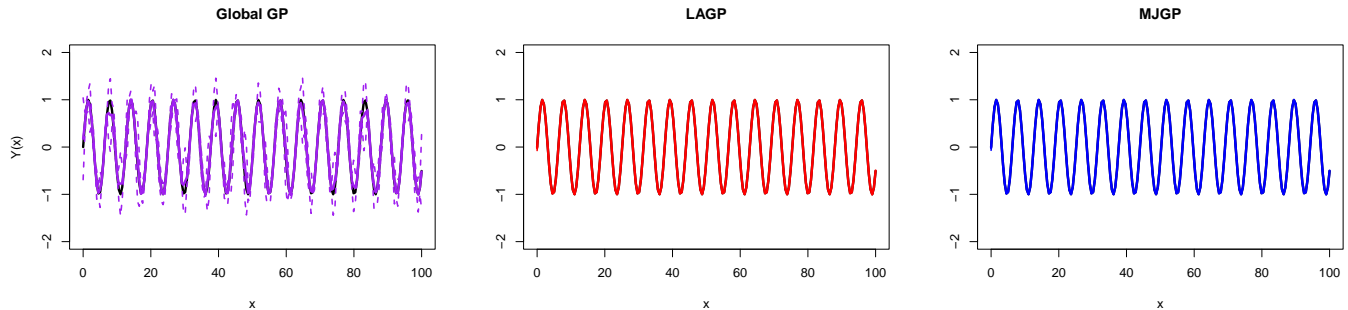


Figure 20: Predictive mean and 95% PI for the no jump case using a (*left*) global GP, (*center*) LAGP, and (*right*) MJGP.

methods. Since there are no jumps, we do not expect using MJGP to offer any improvements. However, it is worth noting that using MJGP did not hurt us; the predictions made by MJGP are just as accurate as those made by LAGP. We confirm this statement using RMSPE; the global GP, LAGP, and MJGP produce RMSPEs of 0.0678, 0.0017, and 0.0015, respectively. This tells us that the method can be used when jumps are suspected but not confirmed without risk of overfitting.

D Comparison to Partitioned GP

One alternative to MJGP is to partition the input space and then fit separate GPs to each partition. However, we prefer MJGP because these partitions are often difficult for a classifier to learn. Consider again the Phantom data set as an example. In Section 4.1 we fit a classifier mapping X_N to C_N , the likely component membership. Rather than using the predicted probability of component membership as a new feature, we could have partitioned the input space into two regions according to their predicted component. The results of such a classification are shown in the left panel of Figure 21. The manifold of discontinuity is overlaid as a dashed red line. Here we see that the classification does a decent job of matching the outer circle, but struggles to classify the inner circle and ellipses. The top circle is completely misclassified.

Say we were to fit separate GPs based on this partitioning. The results of this method using a global GP and OLAGP are shown in the center and right panels of Figure 21, respectively. In both fits we see the effects of fitting separate GPs; there are jumps along the contours of the classification, even for points on the same side of the manifold of discontinuity. OLAGP offers some improvements over a global GP, but neither performs as well as MJGP; the global GP and OLAGP fits have RMSPEs of 0.1404 and 0.1290, respectively. This is because MJGP is able to incorporate the uncertainty of the classification model, while partitioned GPs ignore this uncertainty.

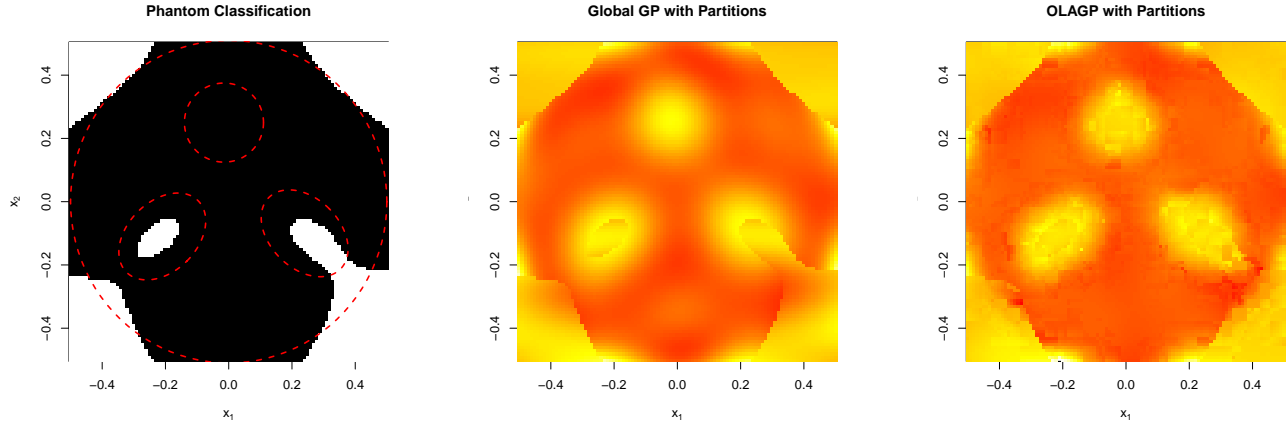


Figure 21: *Left*: Predicted component membership by classification model; *Center*: Global GP fit on partitioned input space; *Right*: OLAGP fit on partitioned input space.

E Computational Time

Table 2 shows the time (in minutes) of each of the simulations in Section 5. We report the computation

Model	Phantom	Star	Modified Michalewicz	AMHV Transport
Global GP	4.92	3.75	N/A	12.87
LAGP	0.02	0.02	0.93	0.06
OLAGP	0.33	0.32	4.85	0.43
OJGP	22.32	22.22	352.95	30.57
MJGP	10.42	13.56	6.13	29.44

Table 2: Computation times for all data sets.

time of a single Monte Carlo iteration since the computation time is not overly variable between reps. Times were recorded on an 8-core, Intel i7 CPU at 3.5GHz. We see that in general, the two JGP methods take the longest, with OJGP consistently taking the longest. This is especially apparent for the Modified Michalewicz function, although we recognize that this could likely be improved by parallelizing the code. We also see from this table that the time required for MJGP is highly dependent on the classification model used. Recall that part of MJGP is a GP fit, either global (AMHV Transport) or OLAGP (all other data sets). So we might expect MJGP to have similar computational efficiency to its corresponding GP method. However, this is not the case for all data sets. MJGP takes quite a bit longer to run than its GP counterparts for all data sets except the Modified Michalewicz function. This extra time is due to the classification model used; we see that MJGP takes longer, in general, when a CGP is used than when a RF is used.

F Prediction Interval Coverage

Figure 22 shows the prediction interval coverage for each of the simulations in Section 5. For each rep of each simulation, we recorded the percentage of true responses that fell within a 95% prediction interval of the predicted mean. We used those percentages to create the boxplots shown, with a dashed line at 95% to represent nominal coverage. For both the Phantom and Star data sets, shown in the left two panels,

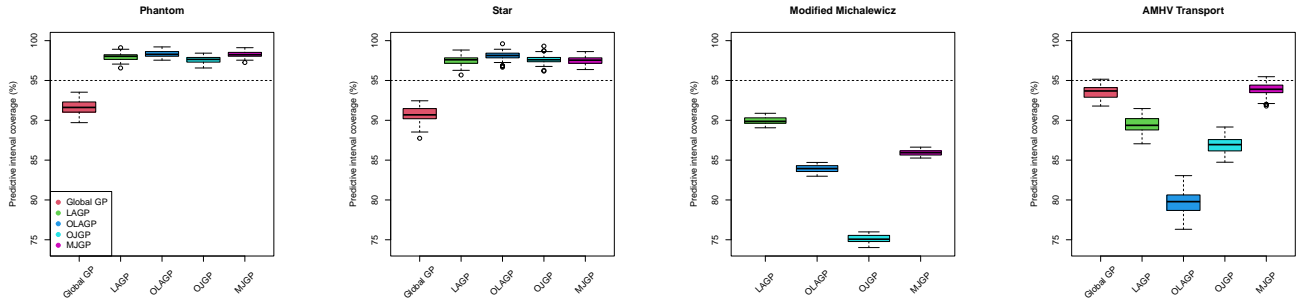


Figure 22: Prediction interval coverage for the (left) Phantom, (left center) Star, (right center) Modified Michalewicz, and (right) AMHV transport data sets.

all methods except the global GP show coverage that is similar to each other but slightly higher than the nominal rate. Higher than nominal coverage indicates that prediction intervals are wider than necessary. This is a potential cause for concern, but since coverage is similar for all methods we prefer the method that produces the lowest RMSPEs, MJGP.

The results for the Modified Michalewicz and AMHV Transport data sets, shown in the right two panels, show a different trend. Here we see that all methods have lower than nominal coverage. Starting with the Modified Michalewicz data set, we see that OJGP, in addition to having the highest RMSPEs, also has the worst interval coverage of all methods. Similarly, OLAGP, which had the second highest RMSPEs, also has the second lowest interval coverage. LAGP, although having higher RMSPEs than MJGP, has better interval coverage. So LAGP may be preferable to MJGP for the Modified Michalewicz data set depending on the task at hand.

For the AMHV Transport data set, we again see that all methods undercover, but to a lesser extent than for the Modified Michalewicz data set. Here we see OLAGP produces the lowest interval coverage, which again matches the RMSPE trends we saw. We suspect this is caused by the aforementioned issues of OLAGP with sparse data. LAGP is less affected by these issues, showing better coverage than OJGP, which had the second lowest RMSPEs but second worst interval coverage. Both the global GP and MJGP have the best coverage, producing (on average) slightly lower the nominal coverage. Since MJGP also produced the lowest RMSPEs, we find that it was the best performing model overall.